Geochimica et Cosmochimica Acta 424 (2026) 194–212

Contents lists available at ScienceDirect

Geochimica et Cosmochimica Acta

journal homepage: www.elsevier.com/locate/gca

Carboxyl-stabilized Mn redox cycling promotes a metastable kutnahorite-to-dolomite pathway

Daniel A. Petrash [a,b,*], Astolfo Valero [b], Or M. Bialik [c,d], Yihang Fang [e], Maartje Hamers [f], Travis B. Meador [b,g], Tomaso R.R. Bontognali [h,i,j], Michael Ernst Böttcher [k,l,m], Oliver Plümper [f,n]

[a] Environmental Geochemistry and Biogeochemistry, Czech Geological Survey, Prague, Czech Republic
[b] Soil Biology and Biogeochemistry, Biology Centre of the Czech Academy of Sciences, Czech Republic
[c] Geology and Paleontology, University of Münster, Germany
[d] Israel Oceanographic and Limnological Research, Israel
[e] Science and Engineering, University of Missouri, Kansas City, USA
[f] Earth Sciences, Utrecht University, the Netherlands
[g] Chemistry, University of South Bohemia, Ceske Budejovice, Czech Republic
[h] Space Exploration Institute, Switzerland
[i] Physical Geography and Environmental Change, University of Basel, Switzerland
[j] Environmental Science Centre, Qatar University, Qatar
[k] Marine Geochemistry, University of Greifswald, Germany
[l] Interdisciplinary Faculty, University of Rostock, Germany
[m] Geochemistry and Isotope-Biogeochemistry, Leibniz Institute for Baltic Sea Research (IOW), Warnemünde, Germany
[n] Faculty of Geosciences, University of Bremen, Germany

ARTICLE INFO

Associate editor: Karim Benzerara

ABSTRACT

Fine-crystalline, fabric-preserving dolostones in deep-time successions are difficult to reconcile with high-temperature burial models, suggesting the existence of a low-temperature formation pathway capable of overcoming both the kinetic hydration barrier of Mg^{2+} and the thermodynamic miscibility gap separating calcite from ordered dolomite. Here, we demonstrate a kinetically favourable route to self-assembling dolomite driven by the synergy of manganese redox cycling and carboxyl functionalization. Using a bio-inspired electrochemical reactor, we show that electrochemical valence-state modulation selectively regulates Mn^{2+} co-precipitation with dolomite reactants. Unlike inorganic controls where manganese is rapidly sequestered into non-templating phases, the functionalized system transiently stabilizes reactive Mn(III) intermediates. This sustains redox cycling and prevents irreversible oxide immobilization, which templates the nucleation of spheroidal, metastable magnesian-kutnahorite. Nanostructural characterization reveals a core–shell architecture where this metastable, isostructural precursor serves as a lattice-distorted scaffold, enabling the rapid heteroepitaxial growth of substitutionally disordered manganoan dolomite cortices. Mechanistically, localized acidity from redox cycling triggers a "proton-driven cation pump", actively releasing Mg^{2+} (and Ca^{2+}) from the functionalized hydrogel reservoir to the mineralization front. This electrochemical route offers an extrapolable geological framework that links the massive fabric-retentive dolostones of the Precambrian to ancient redox-stratified shallow oceans, while explaining their punctuated scarcity in the Phanerozoic as a consequence of global oxygenation decoupling the manganese redox shuttle from shallow-marine environments.

1. Introduction

Despite its global abundance throughout the geological record, the low-temperature formation of dolomite ($CaMg(CO_3)_2$) remains a fundamental problem in carbonate geochemistry (Ingerson, 1962; McKenzie, 1991; Arvidson and Mackenzie, 1999; Pina et al., 2022). At elevated temperatures, ordered dolomite-group carbonates can readily form because thermal activation helps overcome both Mg^{2+} hydration

* Corresponding author at: Czech Geological Survey, Prague, Czech Republic.
E-mail address: daniel.petras@geology.cz (D.A. Petrash).

https://doi.org/10.1016/j.gca.2026.05.034
Received 5 February 2026; Accepted 27 May 2026
Available online 30 May 2026

barriers (Lippmann, 1973; Helm and Merbach, 2005) and cation-ordering constraints (Graf and Goldsmith, 1956; Goldsmith and Graf, 1960), allowing such double-cation carbonate phases to approach equilibrium stability fields (Kaczmarek and Sibley, 2014; Rodriguez-Blanco et al., 2015; Kaczmarek and Thornton, 2017). Under near-surface conditions, however, these barriers become severe. Kinetic effects promote the persistence of metastable carbonate compositions (Thortenson and Plummer, 1977; Mucci, 2004). Mg^{2+} hydration inhibits incorporation into the growing lattice (Lippmann, 1973), while the miscibility gap between Ca-rich metastable phases and ordered dolomite-group carbonates imposes an additional thermodynamic discontinuity that widens at low temperature (Goldsmith and Graf, 1960). Together, these kinetic and thermodynamic constraints define the "dolomite problem" (Petrash et al., 2017).

These constraints are challenged by syndiagenetic fine-crystalline, fabric-retentive dolostones in deep-time successions. Their relict textures and phantom structures (Weber, 1964), commonly associated with inner-shelf evaporative settings, indicate an early precipitation pathway that differs from the high-temperature diagenetic models often invoked to explain the occurrence of replacive coarse-crystalline dolostones (Hood et al., 2011; Chang et al., 2020; Ren, 2025). Despite the prevalence of these stoichiometric and often fairly ordered phases in the ancient geological record, replicating them under experimentally comparable near-surface conditions has remained unattained. A kinetically distinct, low-temperature syndiagenetic route must, therefore, exist (Bontognali, 2019), one that permits solid-state neomorphism (*sensu* Gregg and Sibley, 1984) from a metastable precursor to the double carbonate under dissolution-reprecipitation operating only at submicron scales at the crystal-solution interface (Zempolich and Baker, 1993; Machel, 1997). This implies an ordering pathway in which compositionally coherent mesocrystalline intermediates recrystallize without overprinting primary textural features. Such a mechanism may also account for mimetic dolomitization of delicate Precambrian microfossils (Tucker, 1982).

Microbes have been proposed to overcome the kinetic barriers for dolomite formation twofold: (i) by altering the bulk chemistry of their immediate microenvironment to modulate supersaturation (e.g., affecting pH and alkalinity *via* metabolic processes); and (ii) by providing specific reactive substrates, such as extracellular polymeric substances (EPS), which can bind Mg^{2+} and Ca^{2+} and lower the energy of magnesium dehydration (Bontognali et al., 2010; Zhang et al., 2012a), while also acting as a template for nucleation (Trichet and Defarge, 1995; Wang et al., 2009). Despite extensive research, however, the consensus remains that benthic microbial activity in isolation does not provide a complete solution to the kinetic hurdles of near-surface dolomite precipitation. Experimental synthesis efforts conducted at low temperatures have not yielded ordered dolomite using microbial cultures as the sole kinetic accelerator (Gregg et al., 2015), reinforcing an early notion (i.e., Bischoff, 1968) that additional catalysts, perhaps acting as integrated components of broader biogeochemical systems, are required to simultaneously bridge both thermodynamic and kinetic precipitation barriers.

Beyond microbes and their EPS, a range of other catalysts has been explored in this context, including: (i) organic solvents with low dielectric constants, e.g., dioxane (Oomori and Kitano, 1987), or ethanol (Fang et al., 2022). While not naturally present, these compounds serve as experimental proxies, simulating the Mg-desolvating effects of the hydrophobic, low-water-activity domains found within microbial EPS (Zhang et al., 2012a). Besides highly concentrated salt solutions (Usdowski, 1989), other catalytic agents include (ii) dissolved silica (Fang and Xu, 2022; Al Disi et al., 2024); (iii) sulfide (Zhang et al., 2012b)—a primary byproduct of sulfate-reducing bacteria; (iv) ammonia (Meng et al., 2024), originating from metal-coupled microbial nitrogen respiration (Slaughter and Hill, 1991; Petrash et al., 2025); and (v) bioessential trace elements like zinc (Vandeginste et al., 2019), which acts as a metal center in microbial enzymes crucial for regulating carbonate speciation (Silverman and Lindskog, 1988). Among the array of potential catalytic agents, (iv) Mn distinguishes itself through a unique, multi-modal capacity to potentially drive dolomite formation. This includes redox-controlled alkalinity production and proton consumption (Petrash et al., 2015), cell surface-templating (Daye et al., 2019), and ionic lattice distortion (Han et al., 2024).

A structural solution emerges in the Ca–Mg–Mn ternary carbonate system, where Mn-bearing carbonate phases may provide an intermediate crystallographic bridge between calcite-type precursors and dolomite (Reeder, 1983; Peacor et al., 1987). Kutnahorite is isostructural with dolomite, but substitution of Mn^{2+} (0.83 Å) for Mg^{2+} (0.72 Å) at the smaller B site expands the carbonate lattice, offering one possible crystallographic route by which metastable Ca–Mn±Mg carbonate precursors (Rosenberg and Foit, 1979; Peacor et al., 1987) may evolve to Mn-bearing dolomite. Such Mn-rich, nanocrystalline scaffolds could in turn lower the energetic penalty associated with cation ordering in the dolomite motif, consistent with earlier observations of transient Mn-rich double carbonate intermediates during manganoan calcite precipitation (Mucci, 1988).

From a non-classical crystallization perspective, these Mn-rich precursors may promote dolomite formation through semi-oriented mesocrystal attachment and heteroepitaxial overgrowth. Rather than requiring ion-by-ion addition across a compositionally discontinuous interface, pre-formed nanocrystals sharing a common carbonate framework can aggregate in near-crystallographic alignment and mature toward more ordered products (Cölfen and Mann, 2003; De Yoreo et al., 2015; Putnis et al., 2021; Meister, 2025). This pathway is mechanistically significant because Mg^{2+} incorporation at step edges is inhibited by its high dehydration energy, causing step pinning and limiting sustained layer propagation (Higgins and Hu, 2005). A kutnahoritic scaffold may bypass this barrier by providing a more permissive Mn-expanded template for subsequent Mg incorporation, consistent with enhanced carbonate growth kinetics in Mn-bearing protodolomite syntheses (Han et al., 2024). In this view, Mn^{2+} acts not as a passive substituent, but as an active structural mediator that stabilizes metastable intermediates and opens ordering pathways otherwise inaccessible under low-temperature conditions (Daye et al., 2019).

Here, we experimentally test this hypothesis and establish falsifiable criteria using a bio-inspired electrochemical reactor that simulates quasi-reversible Mn(II) ↔ Mn(III) redox cycling at carboxyl-functionalized interfaces analogous to those found in shallow-marine (peritidal), Mn-oxyhydroxide-binding microbial mats (e.g., Petrash et al., 2015). These dolomite-forming depositional systems are characterized by diurnal redox oscillations (Jørgensen et al., 1979) and electrogenic microbial activity (e.g., Nielsen et al., 2010), which can generate potential gradients comparable to those experimentally imposed here.

Using alginate, a chemically defined proxy for EPS (Petrash et al., 2011), also exhibiting conductivity imparted by metal crosslinking (Ji et al., 2022), we show that sustained Mn redox cycling stabilizes reactive Mn(III) intermediates via inner-sphere complexation with carboxyl groups, suppressing their disproportionation and immobilization (Luther, 2005), thus transforming the organic matrix into an active kinetic mediator. Mechanistically, this mediator functions as a proton-driven cation pump. Localized acidification driven by Mn(II) oxidation "depins" Mg^{2+} and Ca^{2+} complexed in the hydrogel, concentrating them at the mineralization front. This active mobilization, buffered by proton-consuming Mn-reduction cycles, drives the rapid nucleation of spheroidal magnesian-kutnahorite as a metastable precursor, which serves as an epitaxial scaffold, lowering the kinetic barrier for the subsequent rapid crystallization of disordered dolomite.

This electrochemical mechanism provides a framework for explaining the paragenesis of delicate, fabric-retentive dolostones observed throughout the rock record. We propose that this coupling, linking manganese availability to precursor dolomite precipitation, was a fundamental driver for the massive, basin-wide fabric retentive

dolomicrite facies characteristic of the Precambrian. By identifying this catalytic engine, we propose an explanation for the secular distribution of massive dolomite in the Phanerozoic sedimentary rock record as the result of the spatial (de)coupling of manganese redox cycling from shallow carbonate platforms.

2. Methods

2.1. Precipitation setup

The experimental design comprises an H-cell electrochemical system (150 mL borosilicate glass reaction vessels) connected to an automatic titrator (SI Analytics Titroline 7000). The electrochemical system was filled with 125 mL of 80 mM $NaHCO_3$ electrolyte solution, and its cells were separated by an anion exchange membrane (Fumasep® FKE-50, Fumatech GmbH) and were continuously stirred at 250 rpm via synchronized MIXDrive stirrers (2Mag). One cell was open through a 0.2 μm cellulose acetate filter to maintain the dissolved inorganic carbon of our electrolyte in equilibrium with the atmosphere at 25°C. The headspace of the other cell was kept anoxic by a constant flow of argon, initiated 5 min before experiments. In the anoxic cell, a graphite rod working electrode (WE, CP-2200, CP-Graphitprodukte GmbH) and an Ag/AgCl reference electrode (sat. KCl, +197 mV *vs.* standard hydrogen electrode (SHE); RE-1B, ALS Japan) were inserted. In the oxic side of the cell, another graphite rod was used as the counter electrode (CE). A schematic representation of the electrochemical system is shown in Fig. 1.

In a subset of experiments, Na-alginate (300 $mg{\cdot}L^{-1}$, Sigma-Aldrich) was premixed with the electrolyte before reaction to assess the effect of carboxyl functionalization. Alginate is a carboxyl-rich polysaccharide and a key EPS component in microbial mats colonizing hypersaline, dolomite-forming settings (Mercedes-Martín et al., 2016). At environmentally relevant pH values above its p*Ka*, alginate carboxyl groups are deprotonated and can crosslink with metal ions to form hydrogels (Petrash et al., 2011). Such metal-crosslinked hydrogels can exhibit enhanced ionic/electronic conductivity (Ji et al., 2022), providing a chemically defined proxy for carboxylated, electroactive EPS matrices. Since the concentration of alginate employed here is insufficient to substantially alter bulk electrolyte conductivity relative to the 80 mM $NaHCO_3$ background electrolyte, the electrochemical responses observed are attributable to the interfacial carboxyl chemistry rather than bulk solution effects.

To isolate the effects of organic functionalization and electrochemical modulation on mineral formation, four experimental conditions were tested: **(E_{00})** control, lacking both functionalization and electrochemical modulation, served as the baseline for surface precipitation; **(E_{10})** carboxyl-functionalized without electrochemistry, this condition isolated the effect of the carboxyl groups on mineral formation in the absence of an applied potential; **(E_{01})** a non-carboxyl-functionalized sample was subjected to electrochemical modulation to assess the role of redox cycling in the absence of the biopolymer; **(E_{11})** a carboxyl-functionalized surface with an applied electrochemical treatment to evaluate potential synergistic or antagonistic interactions. All conditions were conducted in duplicate. Deionized water (18.2 $M\Omega{\cdot}cm^{-1}$) and analytical-grade reagents were used to prepare all solutions.

2.2. Electrochemical precipitation protocol

During each experimental run, an initial pH value of 8.5 ± 0.1 in the anodic cell was raised to 9.1 units after additions of 100 to 200 μL of 0.5 M NaOH solution as pre-titrant. Following pre-titration, a cation feedstock (0.6 M (Ca,Mg)Cl_2; Ca:Mg = 1:6) was dosed into the anodic chamber at a rate of 1 $mL{\cdot}min^{-1}$ for 20 min (20 mL total); the final working volume of the H-cell setup was 145 mL. The electrolyte pH was maintained at 9.2 ± 0.4 by automatically dosing the titrant into the anodic cell (1.2–3.0 mL in total) using the automatic titrator in pH-stat mode. The experimental pH envelope was selected to replicate the upper range of pH values documented in modern, dolomite-forming environments such as hypersaline coastal lagoons and alkaline lakes where syndepositional dolomite formation is actively occurring (e.g., Warren 1990; Petrash et al., 2015; McCormack et al., 2018). This was done while also maintaining sufficient CO_3^{2-} activity to sustain the thermodynamic driving force for carbonate phase nucleation. The pH-stat design maintained the experimental envelope throughout each run, ensuring that

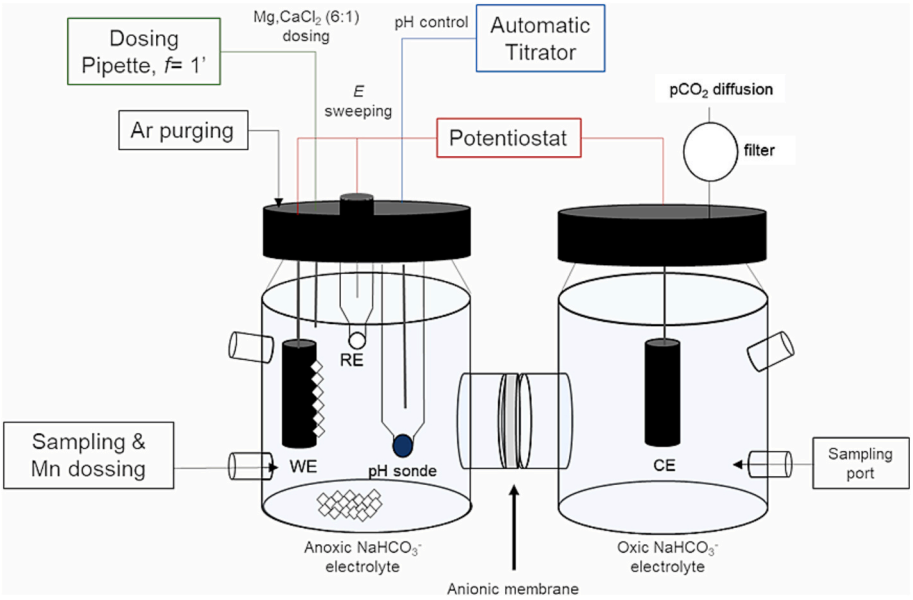

Fig. 1. Schematic of the two-cell electrochemical precipitation apparatus. Two 150 mL borosilicate glass reaction vessels were connected via an anodic membrane. System hydrochemistry was controlled using an automatic pH-stat titrator and a potentiostat applying continuous potential sweeps. One cell, containing the working electrode (WE) and reference electrode (RE), was maintained under an Ar atmosphere, while the other, housing the counter electrode (CE), remained in equilibrium with air. The WE had an electrochemical surface area of 10.9 cm^2. The electrolyte consisted of $NaHCO_3$ solution. Following pre-titration (see text for details), the cation feedstock was introduced at 1′ intervals using a dosing pipette (n = 20); a single $MnCl_2$ dose was at t_0. The inset shows WE and surface precipitates, with residual precipitates formed quasi-instantaneously in solution upon reactant additions. This study focuses on the surface precipitates.

differences in solid-phase outcomes across the four conditions are attributable solely to the primary experimental variables: (i) Mn redox cycling and (ii) carboxyl functionalization, rather than to pH drift.

Before cation feedstock dosing, a single addition of $MnCl_2$ stock solution was added to the anodic cell to achieve a Mn concentration of 10 mM. After five doses, supersaturation with respect to Mg-Ca phases but undersaturation for Mn-precursors is predicted by mineral speciation modelling (Table S1). Concurrently with reactant dosing, oscillations in the redox potential of the electrolyte were induced by using a Dropsens μStat 8000 multichannel potentiostat (Metrohm) in cyclic voltammetry mode (CV) for 28 min. The electric potential was continuously swept between −0.1 and 0.5 V at a scan rate of 2 mV s^{-1}. This environmentally relevant Eh window (e.g., Jørgensen et al., 1979; Di Loreto et al., 2021) targets the Mn(II)/Mn(III) couple, driving oxidative cycling at the periphery of the working electrode (WE) without inducing water hydrolysis or insoluble Mn(IV) oxide precipitation. It aligns with a physicochemical condition in the nitrogenous and manganous zone where incomplete manganese cycling is thermodynamically dominant (Petrash et al., 2025). After titration, the electrolyte solution in the anodic cell was left undisturbed for 24 h to permit stabilization of the surface precipitates. Following this step, the WEs were retrieved, disassembled, and stored under anoxic conditions until solid-phase characterization.

Electrochemical data processing was as follows. Current–time data provide the magnitude of the electrochemical response for each cycle. The maximum and minimum currents extracted from the time-domain measurements provide the anodic and cathodic anchors for constraining the voltammetric response, which is converted to current density using an electrochemical surface area of ~10.9 cm^2 (this includes geometric, microscale surface roughness and micropore areas). Potentials are referenced to the SHE. Anodic and cathodic sweeps were then separated and interpolated onto a common potential grid, enabling direct point-by-point comparison between forward and reverse scans. Residual offsets were minimized by aligning the anodic and cathodic branches while preserving cycle-to-cycle drift across successive scans. This processing enabled direct calculation of the difference between anodic and cathodic current densities at a given potential $\Delta j(E) = j_{an\ (Mn(II)\rightarrow Mn(III))} - j_{cat\ (Mn(III)\rightarrow Mn(II))}$, while yielding voltammograms suitable for analysis of Mn redox behaviour in the alginate-bearing electrolyte.

2.3. Solution cation concentration determinations

Samples used to monitor the electrolyte's reactant composition were collected from the anoxic chamber at three distinct experimental stages: **(S_i)** t_0 + 5 min **(S_{ii})** t_0 + 20 min; and **(S_{iii})** after the 24 h stabilization period. The aqueous samples were immediately acidified with HNO_3 (trace grade, Sigma-Aldrich). The cations cross-linking alginate are fully recovered after acidification, and the concentrations of Ca^{2+}, Mg^{2+} and Mn^{2+}, relative to the total analyte added to the system, were determined using a triple quadrupole inductively coupled plasma mass spectrometer (ICP-MS; Agilent 8800). Precision was verified against certified standards, and the relative standard deviation was <10% of the reported value for all measurements.

2.4. Multiscale microscopy and nanoscale characterization

Electron-transparent lamellae of surface precipitates were prepared for (scanning) transmission electron microscopy ((S)TEM) using a Helios Nanolab G3 (Thermo Fisher Scientific) focused ion beam scanning electron microscope (FIB-SEM) at the University of Utrecht. This instrument was also employed to assess the micrometre-scale morphological features of the precipitates. Sub-micron scale imaging of lamellae, with thicknesses ranging from 250 to 300 nm, was conducted in bright-field (BF) TEM, dark-field (DF) TEM, and high-angle annular dark field (HAADF) STEM modes. These were performed using either a Thermo Fisher Talos F200X coupled to a Super-X detection system, or a Spectra 300 instrument, operated at accelerating voltages of 200 kV and 300 kV, respectively. Additionally, TEM-coupled energy-dispersive X-ray spectroscopy (EDS) was employed to map the spatial distribution of Mn, Ca, and Mg within sacrificial areas of the precipitates. Selected area electron diffraction (SAED) and electron energy loss spectroscopy (EELS) were further conducted in multiple regions of interest to resolve crystallographic and compositional features of the precipitates at the nanoscale. Dual-EELS datasets (core- and low-loss regimes) were acquired in the Spectra 300 using a CCD camera and DigiScan within the Gatan microscopy suite, with a dispersion of 0.15 eV/pixel and a convergence angle of 0 mrad. The low loss spectrum was used to align the core region and evaluate the lamella thickness. To estimate the manganese valence state, we employed (i) semi-quantitative background-subtracted white line intensity ratios (L_3/L_2) and (ii) the deep-learning spectral decomposition framework MnEdgeNet (Ji et al., 2023). Spectra were analyzed using the noise-free model to strictly constrain oxidation states based on peak position and shape.

3. Results

3.1. Response to titration and electrochemical treatments

Titration data (Fig. 2) show that control samples (E_{00}) required maximal external neutralization due to unbuffered proton release during carbonate precipitation. Conversely, potential sweeping alone (E_{01}) decreased titrant demand. In E_{01}, proton-coupled electron transfer partially offsets the release associated with precipitation, explaining the reduced external titrant demand observed in the electrochemical condition (Eq. (1):

$$Mn^{III}(OH)_{org} + e^- + H^+ \rightarrow Mn^{II}_{org} + H_2O \quad (1)$$

The attribution of this effect to cathodic proton consumption is established by the comparative experimental design, wherein E_{00} isolates the carbonate-precipitation proton flux as an unmodified baseline (Fig. 2), so the differential titrant demand between E_{01} and E_{00} represents the net proton consumption from electrochemical Mn(III) reduction.

The carboxyl functionalization alone (E_{10}) provided intrinsic buffering capacity, attributed to carboxyl groups in the electrolyte solution ($pKa \sim 4$; Petrash et al., 2011). At the experimental pH, the carboxyl-rich biopolymer forms a cation crosslinked hydrogel. As carbonate mineral nucleates, it pulls CO_3^{2-} from the equilibrium, forcing the deprotonation of HCO_3^-. This locally weakens the bond between metals, M, cross-linking the hydrogel at the crystal growth front, releasing the cations back into solution right at the interface of the growing mineral phase (2).

$$R\text{-}COO\text{-}M\text{-}OOC\text{-}R + H^+ \rightarrow R\text{-}COOH + M^{2+} + {}^-OOC\text{-}R \quad (2)$$

The combined system (E_{11}) achieved maximal pH buffering capacity by synergizing active cathodic reduction with passive hydrogel buffering. This dual mechanism effectively mitigated the interfacial acidification front driven by rapid carbonate nucleation, resulting in minimal net titrant consumption (Fig. 2) during the active cation feedstock addition stage.

3.2. Mn redox features developed during electrochemical carbonate synthesis

The system exhibited reproducible periodic current oscillations aligned with successive 4 min potential cycles, where each cycle (corresponding to a full sweep) is characterized by sharp anodic and cathodic spikes (Fig. 3A). Both replicates show consistent current–time domain responses, with a progressive attenuation of peak amplitudes upon continued cycling.

In cyclic voltammetry (CV), experiments lacking Na-alginate, i.e.,

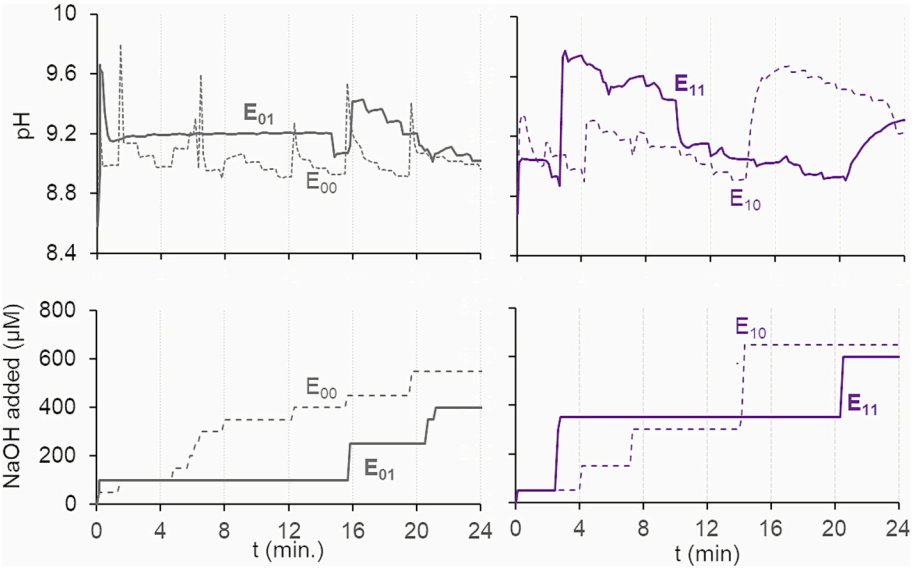

Fig. 2. Experimental pH and NaOH additions during carbonate synthesis. Four conditions were tested: control (E_{00}), electrochemistry only (E_{01}), functionalized only (E_{10}), and combined (E_{11}). Electrochemistry and functionalization reduced titrant demand, enhancing buffering.

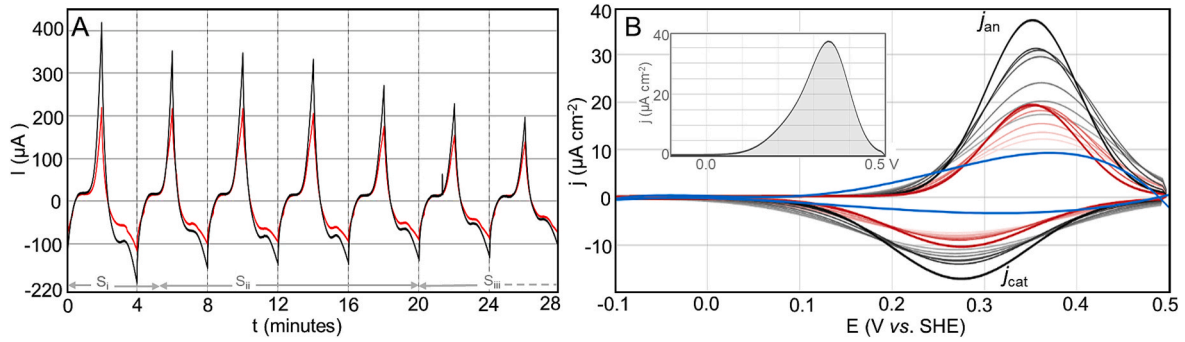

Fig. 3. Electrochemical characterization of Mn redox cycling in the presence of Na-alginate. **(A)** Current–time response showing periodic oscillations over successive 4′ potential cycles with progressive attenuation of current amplitude; experimental stages S_i to S_{iii} are shown. **(B)** Cyclic voltammograms (−0.1 to +0.5 V *vs.* SHE) showing Mn redox features; non-faradaic baseline overlaid to separate capacitive and faradaic contributions J_{an} reaction: $R - Mn^{2+} + H_2O \rightarrow R - Mn^{3+}{-}OH + H^+ + e^-$; J_{cat} reaction: $R - Mn^{3+}{-}OH + H^+ + e^- \rightarrow R - Mn^{2+} + H_2O$, where R is a carboxyl ligand in alginate within the electrolyte. The inset shows the potential-dependent difference current $\Delta j(E) = j\text{an} - j\text{cat}$, highlighting anodic–cathodic asymmetry.

non-functionalized, display negligible faradaic activity within the explored potential window and are dominated by non-faradaic double-layer charging currents, yielding a featureless capacitive profile with no discernible redox peaks (Fig. 3B, blue response). This response defines the background in alginate-bearing experiments. Upon carboxyl functionalization of the electrolyte, a distinct faradaic response emerges in the background-subtracted signal, with a consistent anodic peak at ~0.34–0.35 V *vs.* SHE and a broader, lower-magnitude cathodic counterpart at ~0.28–0.30 V *vs.* SHE (Fig. 3B). The persistence of a paired anodic–cathodic response indicates continued redox cycling, with decline in peak current and baseline-corrected charge density being consistent with progressive depletion of the active electroactive species (Mn(III)/Mn(II)). Preservation of overall CV shape concurrent with monotonic amplitude loss also points to progressive WE passivation. As Mn is progressively incorporated into a newly formed solid-phase reservoir at/near the electrode surface, the growing mineral also decreases electron-transfer accessibility. Mineral textures were assessed using electron microscopy (section 3.4).

Peak faradaic current density decays from cycle 1 to cycle 7 ($\Delta j(E) \approx$ 20 to 30 μA and $j_{an}/j_{cat} \approx 1.2$–$1.4$ across the Mn redox window (Fig. 3B). The persistent anodic bias in $\Delta j(E)$ and j_{an}/j_{cat} deviation from unity indicate departure from nernstian reversibility, reflecting coupled chemical processes at the interface (Bard and Faulkner, 2011). Given the non-faradaic response in alginate-free controls, this result is consistent with redox cycling coupled to interfacial cation binding and release processes.

3.3. Composition of the reactive solutions

As specified in Section 2.3, three sampling stages were defined to capture the chemical evolution of the electrolyte. S_i, collected immediately after 5 doses of cation feedstock ($[Ca]_{dosed} \approx 3.6$ mM, $[Mg]_{dosed} \approx$ 21 mM, [Mn] ≈ 10 mM); S_{ii}, collected at the end of the complete 20-dosed feedstock addition and pH-stat titration ($[Ca]_{dosed} \approx 14$ mM, $[Mg]_{dosed} \approx 86$ mM); and S_{iii}, collected after the 24 h stabilization period. Analytical results for Mg^{2+}, Ca^{2+}, and Mn^{2+} across the four experimental conditions are detailed in Table 1 and illustrated in Fig. 4.

3.3.1. Magnesium removal: kinetic enhancement

Mg removal initiated only after $t_0 + 5$ min, with concentrations at S_i (Fig. 4A, leftmost group) being below quantification limit across all conditions. By the conclusion of the active synthesis stage S_{ii} (Fig. 4A, central group), between 8.7 ± 1.1% (E_{10}) and 28.0 ± 1.0% (E_{01}) of total Mg^{2+} added had been removed, with electrochemical treatment

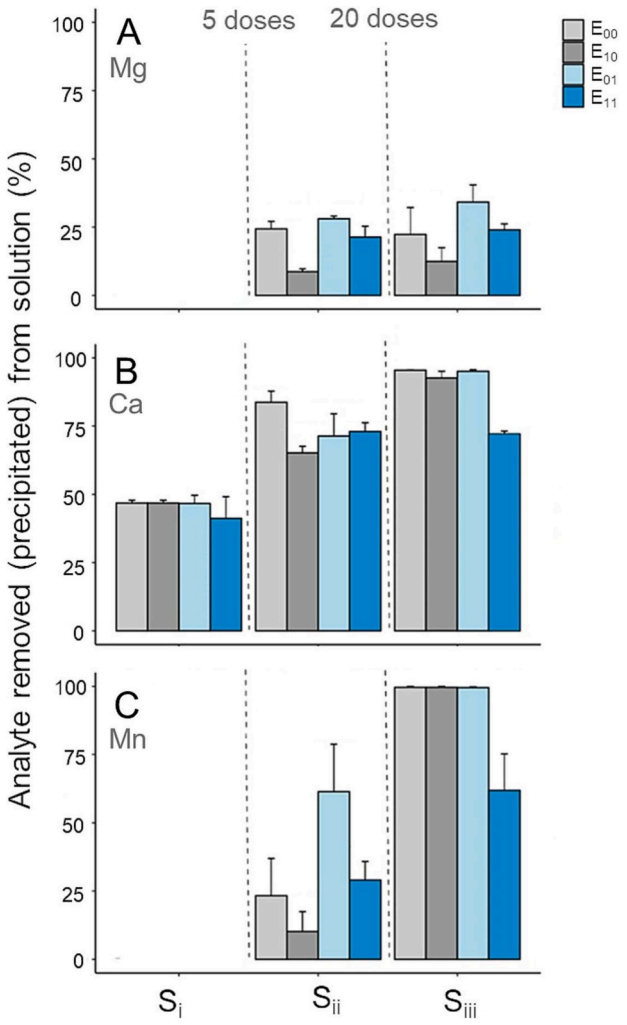

Fig. 4. Quantitative assessment of cation sequestration dynamics across discrete experimental stages and conditions. Comparative analysis of removal percentages for (A) Mg, (B) Ca, and (C) Mn relative to the total molar mass of each cation added. Data are organized into three temporal clusters: the leftmost group represents stage S_i (collected after 5 initial doses), the central group corresponds to stage S_{ii} (at the conclusion of the 20-dose synthesis), and the rightmost group depicts stage S_{iii} (following the 24 h stabilization period). The experimental conditions are differentiated by color-coded bars: light grey signifies the abiotic control (E_{00}); dark grey represents the functionalized-only system (E_{10}); light blue identifies the electrochemical-only treatment (E_{01}); and dark blue denotes the combined functionalized-electrochemical environment (E_{11}). Vertical dashed lines indicate the specific dosing milestones (5 and 20 doses), highlighting the distinct induction of Mn and Mg mineral incorporation post-$MnCl_2$ addition. Consumption was calculated as the percentage difference between measured concentrations and maximum expected concentrations, i.e. @5′ {$[Mg]_{max}$ = 21 mM, $[Ca]_{max}$ = 3.6 mM, $[Mn]_{max}$ = 10.0 mM}; @20′ and 24 h: {$[Mg]_{max}$ = 86 mM, $[Ca]_{max}$ = 14 mM, $[Mn]_{max}$ = 10 mM}. Bars represent mean duplicate values, and whiskers indicate standard deviation based on duplicate experiments.

consistently enhancing removal relative to passive controls. E_{01} surpassed E_{00} by approximately 22%, while E_{11} achieved intermediate removal; lower than E_{01} but higher than the unfunctionalized electrochemical control E_{10}. After the 24 h stabilization period S_{iii} (Fig. 4A, rightmost group), removal remained incomplete across all conditions, with 66–87% of total Mg^{2+} persisting in solution. Further Mg^{2+} removal from S_{ii} to S_{iii} was sluggish, rising by only 3–6% across all conditions (Table 1).

3.3.2. *Calcium removal: Ca availability as a rate-limiting factor*

In contrast to Mg^{2+}, Ca^{2+} removal was already substantial at S_i, with approximately 47% of total added Ca^{2+} depleted prior to S_{ii}. The S_i's Ca-concentration values were indistinguishable across all four conditions (Fig. 4B). This initial, condition-independent depletion coincides with the formation of a "cloudy" suspension following additions of the cation feedstock. That suspension aggregated as droplets which settled to the bottom of the flasks. Given the negligible Mg^{2+} removal at this stage (Fig. 4A, S_i), the pseudo-homogeneously formed precipitate is more likely a Ca-rich phase that largely excluded Mg^{2+}. The occurrence of aragonite with dypingite assemblage in the residual (bottom of the flask) solid phase (Fig. S1) is consistent with that anticipation. The hydrated Mg-carbonate would have formed under the prevailing saturation state during post-stabilization, S_{iii}, as the Ca-depleted and Mg-enriched residual solution was left to evaporate (Table S1).

By experimental stage II, S_{ii}, Ca removal continued across all conditions (Fig. 4B), reaching 65–84% of total added Ca, with E_{00} showing the highest removal and E_{11} the lowest (~65%). This reflects the highest retention of Ca^{2+} by carboxyl ligand complexation in the functionalized electrochemical condition. Following S_{iii} (Fig. 4B, rightmost group), most conditions exceeded 95% Ca^{2+} removal. The notable exception was E_{11} (~75%) (Table 1). The synergistic effect of the carboxyl ligand field and electrochemical forcing in E_{11} effectively isolated a fraction of Ca^{2+} ions in a non-precipitating state, limiting their availability for |(co) precipitation into carbonate minerals.

3.3.3. *Manganese removal: redox-driven sequestration*

Mn^{2+} concentrations remained unchanged at S_i, suggesting that the first full redox cycle did not produce insoluble Mn-bearing precipitates. By the end of S_{ii} (Fig. 4C, central group), Mn^{2+} removal varied substantially across conditions and showed the strongest dependence on electrochemical treatment. As such, E_{01} achieved 61.4 ± 17.3% removal, far exceeding E_{00} (~23.3%), E_{11} (~29.0%), and E_{10} (10.2%). After the 24 h stabilization period, S_{iii} (Fig. 4C), Mn depletion approached >99% in E_{00}, E_{01}, and E_{10}, indicating near-complete incorporation into solid phases formed under such experimental conditions. The significant exception was E_{11}, where 25–38% of total Mn remained in solution—a paradoxically lower net removal than the unfunctionalized E_{01} despite the applied electrochemical treatment. This reflects stabilization of a fraction of Mn^{3+} within the carboxyl ligand field of the alginate hydrogel (Tordi et al., 2025), which prevents their precipitation while sustaining the quasi-reversible Mn(II) ↔ Mn (III) cycling essential to the templating mechanism (Table 1; Fig. 3A and B).

3.4. *Mineralogical and textural characterization of precipitates*

Neither electrochemical cycling nor functionalization alone produced dolomite-composition-like phases. Control (E_{00}) yielded only minimal, sparse Mn-rich precipitates on the WE (Fig. 5A). Functionalization without electrochemistry (E_{10}) increased precipitate density, forming manganous Mg-Ca carbonate spheroids (Fig. 5B and C). TEM in various modes (Fig. 5D–F) showed that the crystallites comprising those fabrics grow outward from central nucleation points, forming spherulitic structures with radially arranged crystallites.

Electrochemical cycling without functionalization (E_{01}) yielded dispersed aggregates resulting from the rapid coalescence (self-assembly) of multiple nanocrystalline domains. In these experiments, a Mg-carbonate phase forming rosettes was observed in SEM (Fig. 6A). The delicate texture (likely a hydrous phase) was unstable under the ion beam and could not be recovered during FIB-lamella preparation (Fig. 6B). STEM-HAADF imaging reveals that the recovered crystal aggregates exhibited significant internal porosity ("hollow"), consistent with facet-like self-assembly during growth (Fig. 6C). Chemically, these aggregates display a magnesian-calcian rhodochrosite composition. They display distinct zoning indicated by Z-contrast gradients

Table 1
Summary of aqueous geochemical evolution and cation removal efficiencies.

Parameter	Initial Phase (Doses 1–5)	End of titration (20 doses)[†] [‡]	Stabilization 24 h[†]	Primary controlling factors
NaOH Titrant	**Delayed onset:** Lag in consumption (0–15 min) due to proton consumption from Mn(III) reduction	**Linear increase:** Steady demand to buffer proton release from precipitation	**Converged:** Total volume ~ 0.50–0.60 mL (0.25–0.30 mmol-eq OH^-) across all experiments	Proton consumption by electrochemical Mn-reduction *vs.* alkalinity demand from carbonate equilibrium ($HCO_3^- \leftrightarrow CO_3^{2-} + H^+$)
Mg removal	**Negligible:** No significant uptake observed	**Variable:** 8.7 ± 1.1% (E_{10}) to 28.0 ± 1.0% (E_{01}). Highest in electrochemical setups, but reduced by carboxyl (E_{11} < E_{01})	**Incomplete:** Slight increase (3–6%). Majority (66–87%) persists in solution	Electrochemical treatment enhances Mg co-precipitation, but carboxyl functionalization partially mitigates this effect
Ca removal	**Rapid:** >40% removal prior to Mn addition (precursor aragonite formation)	**High:** 65.2 ± 2.4% to 83.7 ± 4.1% removal	**Near complete:** >95% removal, except E_{11} (~75%)	Initial homogeneous nucleation of precursor aragonite; partially inhibited by ligand stabilization in E_{11}
Mn removal	**Not observed:** no insoluble Mn-phase formed upon the initial 5′	**Kinetic Response:** $E_{01} \gg E_{00}$, w./E_{01} (61.4%) > E_{11} (29.0%) > E_{00} (23.3%) > E_{10} (10.2%)	**Complete *vs.* stabilized:** >99% removal in most units. Exception: E_{11} retains 25–38% in solution	Applied potential drives rapid sequestration; alginate in E_{11} stabilizes Mn (III) intermediates against precipitation

[†]Conditions denote E_{00} (control), E_{01} (electrochemistry only), E_{10} (functionalized only), and E_{11} (combined).
[‡]Removal (%)calculated relative to the total molar mass added to the H-cell reactor.

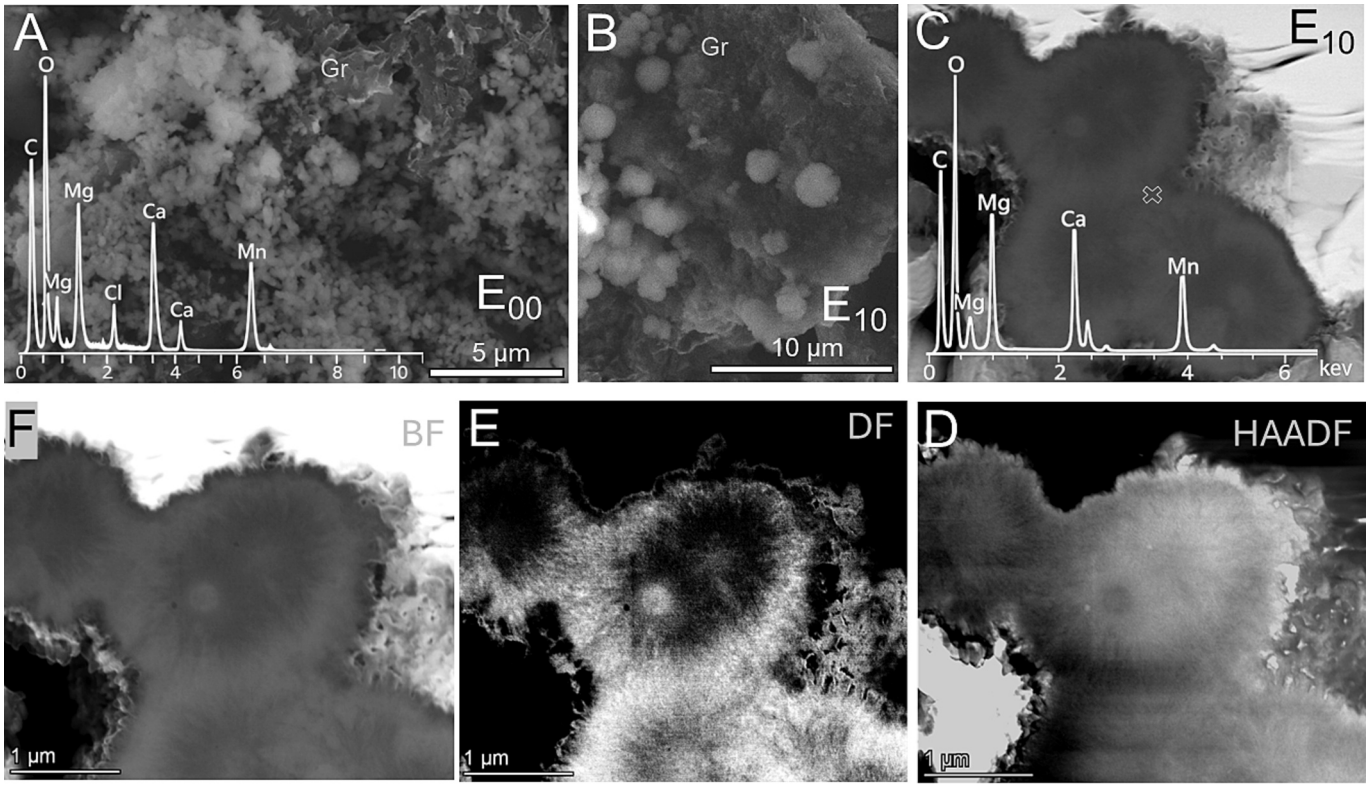

Fig. 5. Solid phase characterization of carbonate precipitates in Control (E_{00}) *vs.* Functionalized (E_{10}) conditions. (A) SEM-EDS characterization of the control sample (E_{00}), where the absence of functionalization and cycling resulted in sparse, Mn-dominated precipitates (Mn ≫ Ca + Mg), and with minimal surface accumulation. (B) SEM image of sample E_{10} (functionalization without electrochemical cycling), showing increased precipitate density and the formation of coherent carbonate spheroids on the graphite (Gr) substrate. (C) EDS spectrum of an E_{10} spheroid (collected in the point marked), confirming the cortical phase as a manganous Mg-Ca carbonate. (D–F) Cross-sectional TEM analysis (HAADF, Dark Field, and Bright Field) of the E_{10} spheroidal fabric shown in "C", revealing the internal fabric is composed of crystallites radiating outward from central nucleation centers.

portraying denser Mn-enriched domains transitioning into Ca-Mg enriched inner domains, and with Mg homogenously distributed along rims (Fig. 6C–E). SAED ring assignments generated a d_{104} spacing of ~2.84 Å, which alongside d_{113} (2.39 Å) and d_{110} (2.16 Å) reflections (Fig. 6F), is consistent with rhodochrosite.

Condition E_{11} yielded more abundant carbonate WE coatings consisting of 1–3 µm polycrystalline spheroidal aggregates (Fig. 7A–C). Internally, these aggregates are defined by the coalescence of smaller (200–600 nm) spheroids with Mn-enriched, thread-like cores and variably Mg-enriched cortices (Fig. 7C–D). TEM-EDS confirms preferential Mn partitioning in the cores, with oscillatory zoning possibly induced by potential swapping (Fig. 7E). To resolve the potential for solid solution extending to the dolomite-kutnahorite series (*cf.* Peacor et al., 1987), we plotted the EDS data on a ternary Ca-Mg-Mn diagram (Fig. 7H). The data reveal a continuous kinetic trajectory where magnesian-calcian rhodochrosite formed in the cores, transitioned into metastable magnesian kutnahorite to manganoan protodolomite cortices. Notably, these intermediate compositions plot within the high-

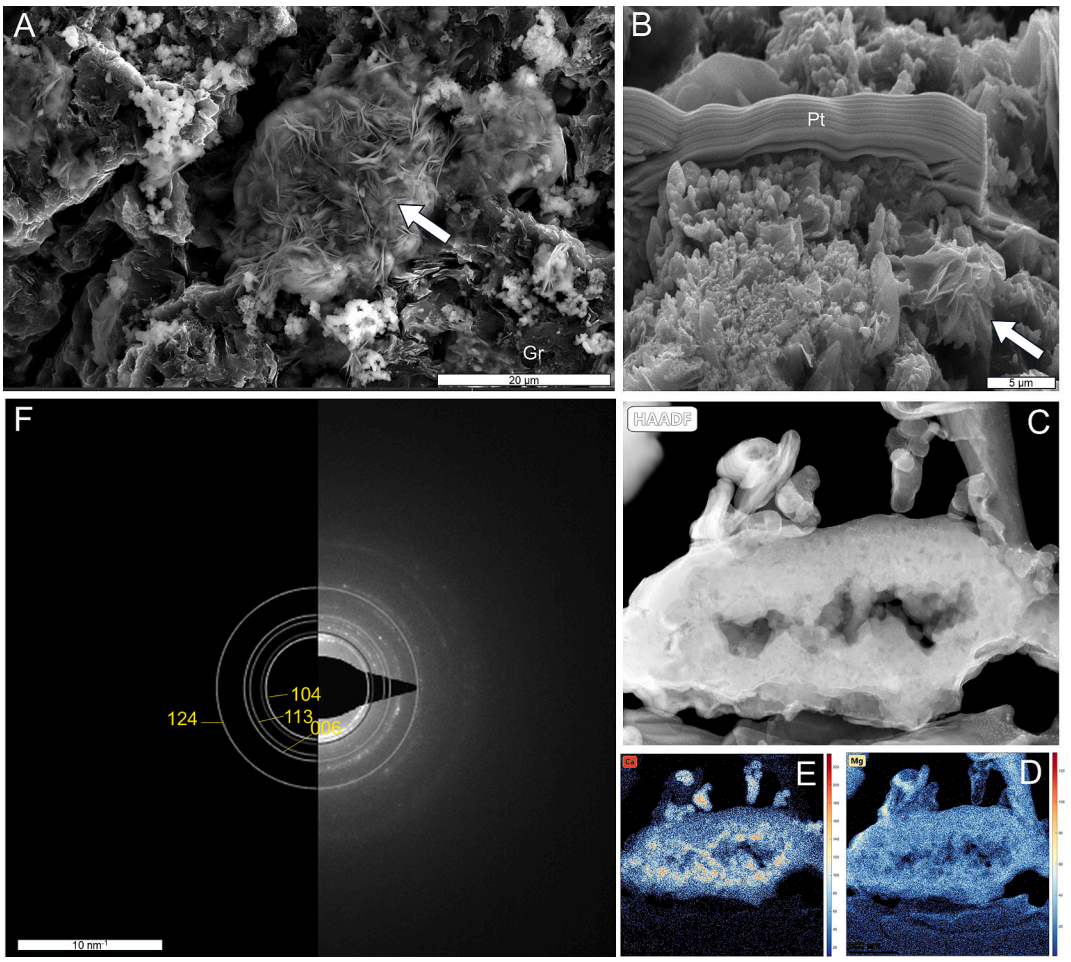

Fig. 6. Morphology and structure of precipitates formed under electrochemical cycling without functionalization (E_{01}). (A) SEM of the electrode surface showing prominent rosette-like structures (arrow) intermixed with disperse, granular polycrystalline aggregates. (B) FIB-milling site; the delicate rosettes (arrow) were unstable under the ion beam, leaving only the granular aggregates for analysis. (C) STEM-HAADF cross-section revealing a porous, "vuggy" texture formed by coalesced nanocrystalline domains. Contrast variations highlight chemical zonation (inset mean EDS spectrum). (D–E) EDS maps contrasting the internal zonation of Ca with the homogeneously distributed Mg. (F) SAED pattern showing diffraction rings consistent with cation-substituted rhodochrosite lattice spacings.

temperature and high-pressure thermodynamic miscibility gap defined by Peacor et al. (1987), where two-phase carbonates are observed along the high-temperature solvus (see also Goldsmith and Graf, 1957). This indicates that rapid kinetic growth stabilizes a continuous solid solution under disequilibrium conditions. It is therefore plausible that semi-coherently intergrown, nanodomain-scale two-carbonate assemblages formed, with a kutnahorite-like phase intergrown with protodolomite (Fig. 7H–I; *cf.* Goldsmith, 1983). In contrast, the E_{01} as magnesian-rhodochrosite products cluster distinctly at the magnesite-calcian rhodochrosite solvus (Fig. 7H); i.e., the crystalline E_{01} phase is presumably stable.

Structurally, HR-TEM reveals that our two-phase manganoan carbonate spheroids possess a mosaic texture composed of nanodomains separated by broad, diffuse low-angle boundaries (Fig. 7F). FFT analysis (Fig. S3) confirms crystallographic misorientations (3–11°) between these regions. Diffraction (Debye-Scherrer) rings in the SAED patterns are inhomogeneous (Fig. 7G) indicative of E_{11} yielding a polycrystalline, randomly oriented precipitate. Overall, the mean measured interplanar distance of the transitional core to cortex zone ($d_{104} \approx 2.93$ Å) is consistent with a disordered Mn-rich Ca-Mg carbonate (pseudo-kutnahorite-like) phase (Mucci, 1988). An interpretation that is further supported by coexisting Ca-Mn-Mg domains within the zoned spherule textures that are compositionally distinct from the Mg-enriched outer cortices (Fig. 7E). The d-spacing in such domains, intermediate between calcite (≈3.03 Å) and rhodochrosite (≈2.84–2.86 Å), are consistent with substantial Mn incorporation into a Ca-bearing carbonate mineral lattice. The cortices, on the other hand, exhibit reflections consistent with a disordered dolomite with near-stoichiometric cation ratio (i.e., Ca: (Mg + Mn) = 1) as per d_{104} *ca.* 2.88 Å. Other reflections that can be confidently assigned to this mineral are d_{101} (4.029 Å), d_{110} (2.404 Å), d_{113} (2.191 Å), and d_{116} (1.786 Å). The characteristic *b*-type superstructure reflections (e.g., d_{015}, d_{021}, etc.), whose presence would signify cation ordering, were unresolved.

3.5. EELS of the cortical precipitates

The results from EELS targeting the synthetic products from E_{11} are shown in Fig. 8A–D. The carbon K-edge spectra are characterized by sharp pre-edge peaks at 290.4 eV and broader features at 300.9 eV, corresponding to the π* and σ* resonances of the C=O bond, respectively. These transitions combined with corresponding O *K*-edges at ~531 eV, uniquely identify the matrix as carbonate (Fig. 8A–B). The Ca $L_{3,2}$-edge (Fig. 8C) shows well-resolved spin–orbit splitting (L_3 at 349 eV), confirming the integration of Ca into a crystal lattice. Most significantly, the spectra capture characteristic Mn $L_{3,2}$-edge features in the 640–650 eV range (Fig. 8D). Mn $L_{2,3}$ edge spectra ($N = 4$) from the core of a representative spheroid were analyzed using the deep-learning MnEdgeNet framework (Ji et al., 2023). The MnEdgeNet modelling results are supplied in Fig. S4. The combined data exhibit L_3/L_2 white line intensity ratio ≈ 2.88 with an L_3 absorption maximum located at

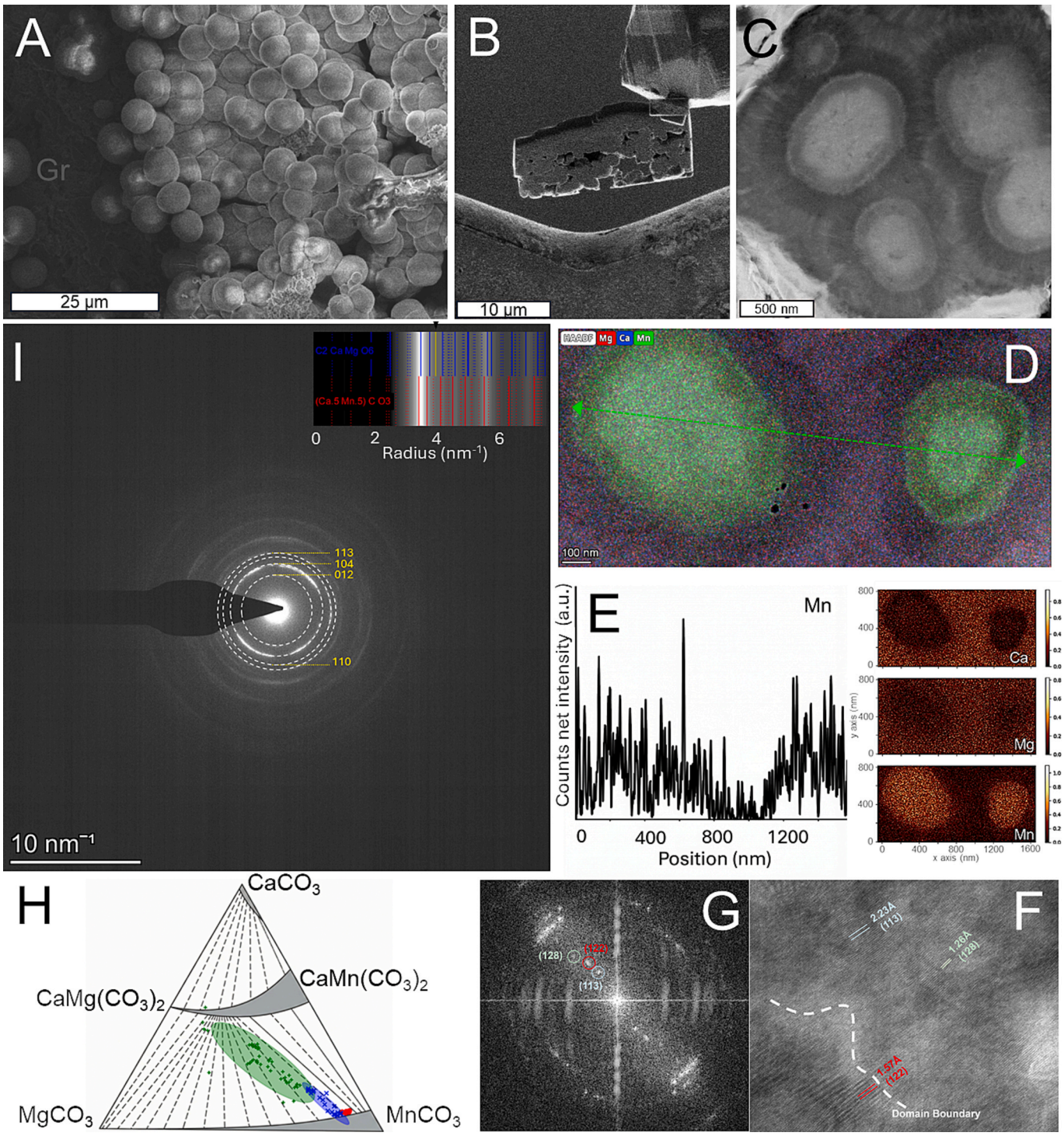

Fig. 7. Multiscale characterization of Mn-templated protodolomite formed under electrochemical and carboxyl modulation (E_{11}). (A–C) Morphology and texture: (A) SEM micrograph showing the dense accumulation of spheroidal aggregates on the graphite electrode (Gr). (B) SEM view of a FIB-milled cross-section (lamella) extracted from the aggregate cluster. (C) STEM-HAADF image of the lamella, revealing the characteristic "eye-like" core–shell zonation and diverging sheaf texture. (D–I) Nanostructure and chemistry: (D) STEM-EDS composite map confirming cation partitioning: Mn-enriched cores (green) surrounded by Mg/Ca-rich cortices (red/blue). (E) EDS line-scan intensity profile (1.6 μm) for Mn across the aggregate (transect in D), showing the preferential sequestration of Mn in the core regions; the segregated distributions of Ca, Mg, and Fe are also shown. (F) High-resolution TEM (HRTEM) micrograph of a crystalline domain. The lattice fringes and the diffuse domain boundary (white dashed line) highlight the mosaic nanostructure, showing nanodomains (<30 nm) intergrown with different crystallographic orientations. (G) Fast Fourier-Transform (FFT) of the HRTEM image (H) Compositional TEM-EDS data projected onto the $CaCO_3$-$MgCO_3$-$MnCO_3$ ternary plot, the low-temperature two-phase manganoan carbonate stability fields/miscibility gap are shown (after Peacor et al., 1987). EDS data renormalized to [Ca] + [Mg] + [Fe] = 1. The confidence ellipses are calculated from the variance (scatter) of the data points. (I) SAED pattern acquired from the cortex with identified diffraction rings. The inset/overlay displays the theoretical ring positions for dolomite and kutnahorite, highlighting the expected location of the d_{015} superstructure reflection. This reflection may be highly attenuated by broadening and superposition of d_{104} peaks in polycrystalline matrices comprising both minerals (see text for details).

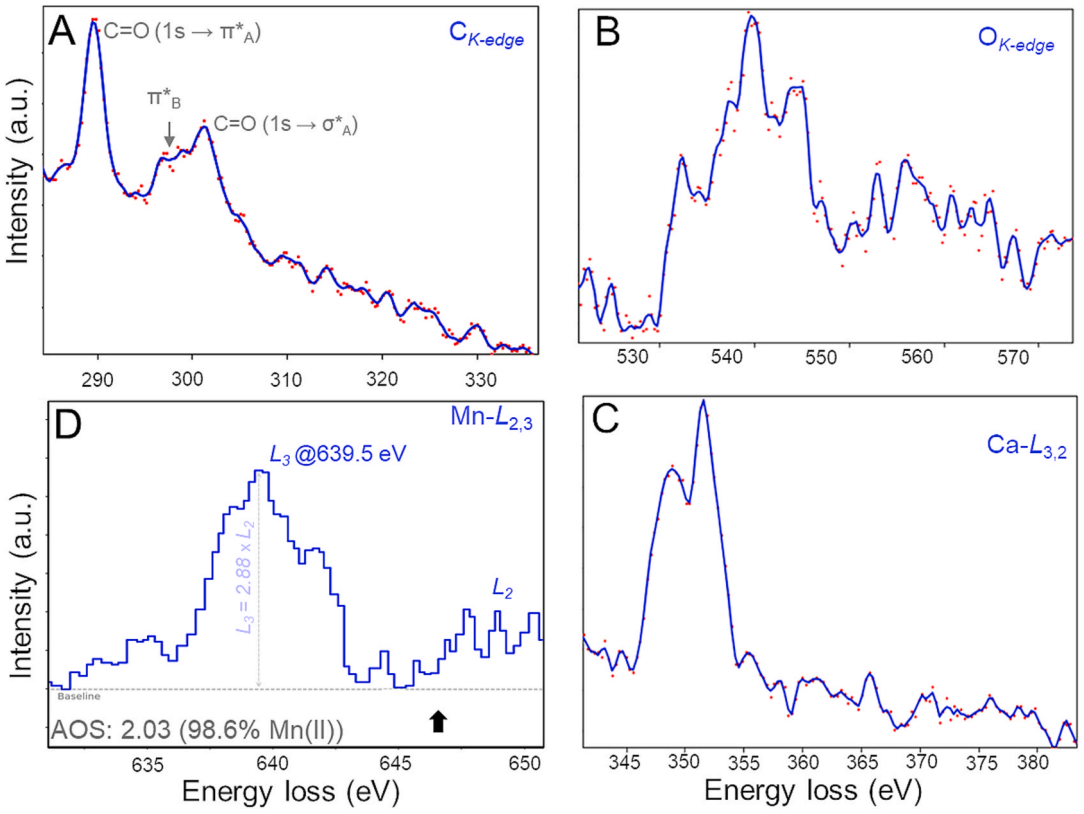

Fig. 8. Representative core-loss EELS spectra acquired from the inner cortex region. (A) Carbon K-edge showing the characteristic π* and σ* transitions of the carbonate. (B) Oxygen K-edge exhibiting fine structure consistent with carbonate bonding. (C) Calcium $L_{3,2}$-edge displaying sharp white lines indicative of a crystalline coordination environment. (D) Manganese $L_{2,3}$ edge spectrum. The data are presented as a raw step plot to preserve peak shape fidelity. The analysis reveals a sharp L_3 maximum at 639.5 eV and an intensity ratio of $L_3/L_2 \approx 2.88$, consistent with high-spin Mn(II). A key feature is the complete return to baseline intensity in the inter-peak valley (~645 eV, black arrow), effectively ruling out significant mixed-valence contributions.

639.5–640.0 eV. The applied MnPredictor decomposition was the 'noise-free' model, which prioritizes peak position fidelity and spectral shape. It returned an average oxidation state of +2.03; indicating ≥98.6% Mn(II) (Fig. 8D). This predominantly divalent state is physically confirmed by the deep spectral valley between the L_3 and L_2 edges (arrow in Fig. 8D), which reaches baseline intensity.

4. Discussion

We present a synthetic route that circumvents the kinetic barriers inhibiting the incorporation of the Mg^{2+} ion in protodolomite by leveraging the redox chemistry of Mn on electrochemically reactive and functionalized surfaces. This result establishes a mechanistic link between dolomite and manganese redox-cycling (Petrash et al., 2015), organic functionalization and ionic lattice distortion (Han et al., 2024), and the increasingly recognized role of electron-transfer mechanisms in marine sediments (Nielsen et al., 2010; Shi et al., 2016). In our chosen experimental system, reactions are confined to interfacial microenvironments where electrochemically driven proton fluxes generate transient and localized departures from the hydrochemistry of the surrounding mother solution. Although the reservoir solution is supersaturated with respect to dolomite (Table S1), the Mn-bearing precursor phase remained undersaturated in the bulk solution (Table S1), indicating that nucleation of the intermediate Mn-rich phase was necessarily restricted to the functionalized electrode interface rather than occurring homogeneously in solution. The experimental design therefore targeted kinetically controlled out-of-equilibrium interfacial processes rather than near-equilibrium precipitation from the surrounding solution. Cyclic voltammetry demonstrates that carboxyl functionalization modulated the electrochemical behavior of manganese, facilitating quasi-reversible Mn(II) ↔ Mn(III) valence state transitions at the WE interface that are otherwise kinetically inhibited. Our central finding is the formation of compositionally zoned spheroids, which featured Ca-Mn-enriched cores and Mg-enriched cortices. The discussion below expands on observations, their interpretations and implications.

4.1. The Mn-templating mechanism

Morphological and nanostructural characterization reveals that low temperature protodolomite formation proceeded via a non-classical, multistep pathway involving a manganous metastable precursor. In the solid-phase products of E_{11}, STEM-HAADF imaging, SAED, and EDS mapping identify Mn-rich cores with rather minor yet increasingly outwards Mg incorporation. These cores serve as epitaxial templates for the subsequent overgrowth of Mg-enriched cortices—a compositional evolution significantly promoted by carboxyl functionalization and potential modulation. The composite E_{11} spheroids have cores analogous to “pseudo-kutnahorite” (Mucci, 1988; Böttcher, 1998), and cortices that are consistent with a manganoan (proto)dolomite precursor, given the absence of ordering reflections.

It is worth noticing, however, that the absence of ordering reflections may be a methodological artifact rather than intrinsic disorder of the products. Relative thickness mapping $(t(\lambda)^{-1})$ derived from the low-loss EELS spectrum reveals that the dolomitic cortices correspond to the thinner regions of the lamellae yet these exhibit local $t(\lambda)^{-1}$ values ranging from 0.86 to 0.88 (Fig. S5). In this regime, approximately 59–64% of the incident electrons undergo inelastic scattering (Egerton, 2011). This substantial background contribution, combined with the polycrystalline nature of our synthetic products, likely lowers the signal-to-noise ratio sufficiently to obscure weak superlattice reflections

possibly associated with incipient cation ordering. Consequently, while the current SAED data are consistent with a disordered precursor, the sample thickness was not optimal for definitively resolving any faint *b*-type reflections characteristic of substantial Ca occupancy in the B site. Attenuation of *b*-type reflections may also be from manganese occupying a substantial portion of the magnesium site within this disordered lattice structure (Peacor et al., 1987).

Although disordered kutnahorite occurs as a metastable phase at near-surface temperatures (Reeder, 1983; Peacor et al., 1987; Mucci, 2004; Böttcher and Dietzel, 2010), our results clearly show that formation of this phase is kinetically favoured over disordered dolomite under functionalized conditions. While thermodynamics alone dictates that dolomite is the more stable phase in our system ($\Delta G^{\circ}_{f\,dol} < \Delta^{\circ}G_{f\,Kutn}$; Rosenberg and Foit, 1979), kinetic factors, specifically those governing the descent of the free energy landscape, ultimately influenced the reaction pathway. In this regard, despite the bulk electrolyte being undersaturated with respect to disordered kutnahorite (SI = −2.57; Table S1), the out-of-equilibrium experiments implemented here indicate that this precursor presents a significantly lower activation energy barrier to nucleation than direct precipitation of oversaturated disordered dolomite (SI = 5.54; Table S1). The result is probably rooted in coordination chemistry, as Mn^{2+} has a lower magnitude of dehydration enthalpy compared to Mg^{2+} (−1851 *vs.* −1926 kJ mol^{-1}; Marcus, 1987), and its water exchange rate is nearly two orders of magnitude faster (2.1 10^7 s^{-1} *vs.* 6.7 10^5 s^{-1}; Helm and Merbach, 2005). This allows Mn^{2+} ions to desolvate and occupy the carbonate lattice rapidly, effectively bypassing the barrier that stalls Mg incorporation (Wogelius et al., 1992).

Other factors may also be at play. The high lattice strain inherent to dolomite (determined by its cationic mismatch ratio, $R_{Ca}/R_{Mg} \sim 1.38$) may contribute substantially to the energetic barrier inhibiting its formation at low temperature. In contrast, within the octahedral geometry, Mn^{2+} possesses an effective ionic radius ~15% larger than that of Mg^{2+} (0.83 Å *vs.* 0.72 Å). This yields a significantly lower mismatch ratio for kutnahorite ($R_{Ca}/R_{Mn} \sim 1.20$) and places the latter phase within a (meta)stability window where lattice strain is sufficiently low to avoid the kinetic penalties that prevent dolomite nucleation and growth. However, lattice-ordering in multicomponent phases is governed by factors beyond simple cation radii (Jakob et al., 2025). In our system, cation-partitioning can also be critical. Mucci (1988) and Böttcher (1998) demonstrated that the Mg distribution coefficient (D_{Mg}) is notably higher in Mn-bearing environments. As the [Mg]/([Mn] + [Ca]) ratio progressively rises during precipitation, D_{Mg} increases, facilitating the incorporation of Mg^{2+} into the Mn-expanded lattice of the kutnahoritic precursor. Being manganoan, this phase, exhibiting a small lattice mismatch (*ca.* 1.5%; a_{Kut} = 4.8732(8) Å, a_{Dol} = 4.8012(1) Å), still has some degree of structural distortion (Rosenberg and Foit, 1979).

HRTEM imaging of E_{11}′s synthetic products reveals that they consist of aggregated nanocrystals with incoherent orientations, possibly implying formation through an assembly of nanoparticle subunits sharing a common crystallographic motif (Cölfen and Mann, 2003). Such variations can force the coexistence of regions with disparate unit cell parameters that may locally exhibit higher-order superstructures (Fang and Xu, 2019; Meister et al., 2023). Forming as the crystal progresses towards a Mg-Ca stoichiometry that is thermodynamically closer to equilibrium, the nanoscale misorientations accommodate lattice misfit (Van Tendeloo et al., 1985). These circumvent the “step-pinning barrier” by stabilizing the strained surface. In the absence of such a favourable isostructural template, the slow dehydration of magnesium leads to strained initial surface layers that undergo rapid monolayer dissolution before stable critical nuclei can grow (Higgins and Hu, 2005). Our results demonstrate that as the isostructural Mn-rich core stabilizes, and the relative Mg^{2+} ion concentration increases, the heteroepitaxial growth of the disordered dolomite cortices on kutnahoritic outer core zones is enabled.

4.2. Carboxyl biomolecules and redox potential oscillations

The nucleation and growth mechanism that we observed is governed by the synergy between organic functionalization and the applied potential sweep. This mimics the interfacial processes active at the reactive surface of sedimentary Mn(IV,III)-bearing phases that can be present in peritidal, chemically stratified dolomite-precipitating depositional systems (e.g., Petrash et al., 2015). The carboxyl acts not merely as a passive template, but as an active agent that modulates, in its interaction with reactive Mn, the free energy landscape, driving the distinct morphological and mineralogical outcomes (Mercedes-Martín et al., 2016).

The interplay between the polymeric matrix and the electric field dictates the growth habit. In the passive functionalized condition (E_{10}), precipitation follows a radial isotropic pathway. The presence of the biopolymer drives supersaturation and nucleation, near the WE surface, occur stochastically from the initial seed. As described by Gránásy et al. (2005), such “non-crystallographic branching disrupts the crystalline anisotropy early in the growth process”, leading to isotropic spherulitic growth.

In contrast, the synergy of carboxyl functionalization and electrochemistry in E_{11} shifts the system toward the Category 2 growth mode of Gránásy et al. (2005), also shifting the reaction profile from thermodynamically to kinetically dominated driving forces (Cölfen and Mann, 2003). In the experimental E_{11} condition, the polarized alginate chains likely establish a directional electric field along the hydrogel, initially inducing a fibrillar habit by (meta)stabilizing metal ions in a dense interfacial pre-nucleation clusters, thus enabling semi-oriented particle attachment—a pathway in which pre-formed nanocrystals adhere in near-crystallographic alignment, establishing small-angle boundaries (De Yoreo et al., 2015; Wolthers et al., 2025).

However, the defining driver is ultimately the evolution of supersaturation near the electrode interface. As the growing spheroids entered a compositional zone where lattice strain blocked classical step-flow mechanisms, the interfacial fluid locally built-up extreme supersaturation. The crystallites are then forced to grow by rapidly incorporating Mg-rich nanoparticle arrays, which resulted in oscillatory zoning (Fig. 7E). This explains the continuous trajectory observed in the ternary plot (Fig. 7H), as rapid kinetic nanoparticle attachment in an increasingly Mg-rich solution possibly captures two metastable phases into the spheroids, effectively bridging the miscibility gap as the solid composition progressively converges upon the double-carbonate stability field (*cf.* Peacor et al., 1987).

4.2.1. The electrochemical “engine”

The (re)oxidation of aqueous Mn(II) requires an inner-sphere mechanism where water is displaced by anionic ligands (Luther, 2005). Alginate carboxyl groups serve this function, partially substituting for water molecules to enable electron transfer to the electroactive manganese reactant (Fig. 9A). As the local activity of Mn^{2+} is progressively decreased, these same ligands transition to binding the increasingly abundant Mg^{2+} ions (Fig. 9B). This chemical evolution in the mother solution is coupled to the solid product via the pre-existing Mn-rich isostructural surface. Driven by ionic radius compatibility and the distribution coefficient (D_{Mg}) covariation (Mucci, 1988; Böttcher, 1998), the pseudo-kutnahoritic core-to-cortex transition served as a lattice bridge that facilitated heteroepitaxy. This mechanism is fuelled by localized interfacial acidification arising from two synergistic sources: (i) carbonate precipitation, and (ii) the stoichiometric proton-release coupled to the incomplete anodic oxidation of Mn(II) (Fig. 3B).

Estimates using a steady-state Nernst approximation suggest this anodic flux induces a local acidification (ΔpH ~ −0.5 to −1.2 units), and probably higher within the diffusion boundary layer at the WE surface (see Note S1 in the Supplementary Data 1). This transiently protonates the carboxyl ligands, locally triggering the “depinning” of crosslinked cations, Mg^{2+}, Mn^{2+}, and Ca^{2+}, which become available for rapid

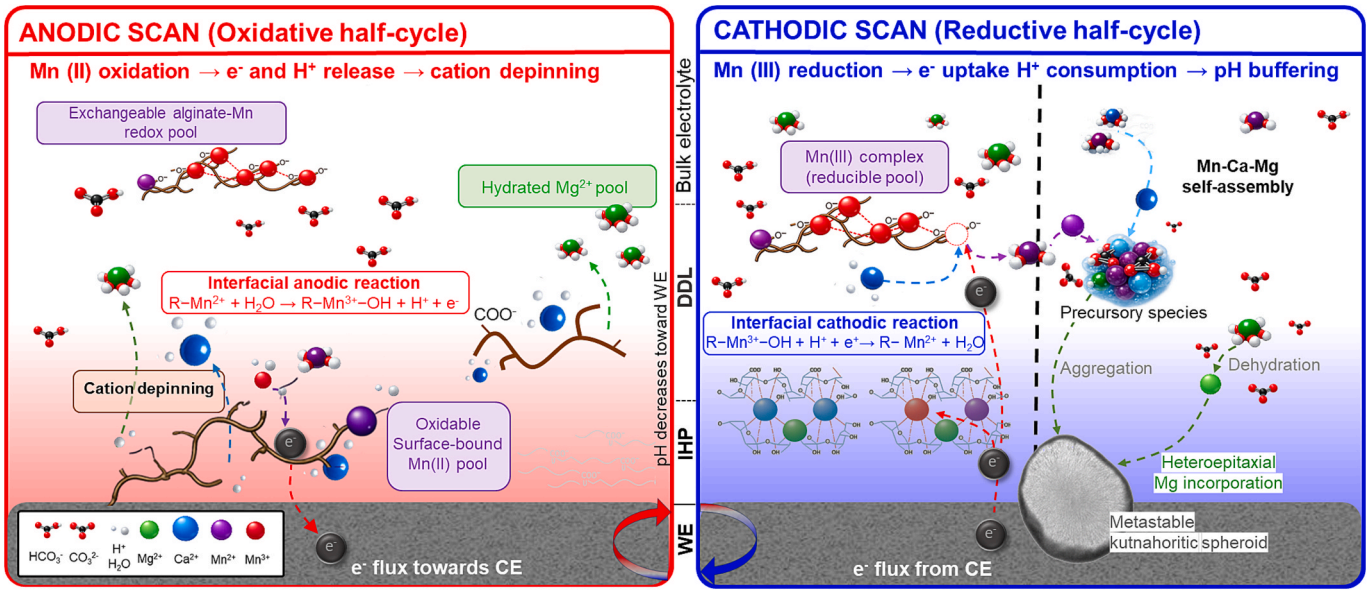

Fig. 9. Conceptual model for the Mn redox–templating mechanism driving low-temperature dolomite nucleation at carboxylated interfaces. During the anodic half-cycle, alginate-bound Mn(II) is oxidized to ligand-stabilized Mn(III), releasing H^+ and generating local acidification at the electrode interface. This proton flux promotes cation depinning/desorption from carboxylated sites, mobilizing Ca^{2+} and Mg^{2+} into the diffuse double layer. During the cathodic half-cycle, ligand-stabilized Mn(III) is reduced back to Mn(II), consuming H^+ and buffering interfacial pH. Together, these alternating redox reactions maintain an exchangeable alginate–Mn redox pool in which Mn(III) is stabilized but remains reducible and available for continued cycling. Repeated proton and electron fluxes sustain non-equilibrium interfacial gradients that promote Mn–Ca–Mg carbonate self-assembly, ligand-assisted dehydration, and formation of hydrated pre-nucleation clusters that transition towards Mn-rich pseudo-kutnahorite scaffolds. These scaffolds provide the isostructural template for subsequent dolomite growth. DDL = diffuse double layer; IHP = inner Helmholtz plane; WE = working electrode; CE = counter electrode.

incorporation into growing cortices (Fig. 9A–B). Transient accumulation of H^+ near the reactive WE surface creates oscillating supersaturation regimes required to stabilize pre-nucleation clusters (De Yoreo et al., 2015); it can also generate oscillatory zoning in the overgrowths (e.g., Katsikopoulos et al., 2009).

Finally, carboxyl functionalization alters the thermodynamic fate of the intermediate Mn species. As delineated by the Eh-pH stability fields (Fig. S6), our experimental conditions (−0.1 to +0.4 V; ~pH ± 1.2 units) oscillate across the critical solubility threshold separating hausmannite (Mn_3O_4) and manganite (MnOOH). The absence of organic ligands results in rapid Mn(III) disproportionation and irreversible precipitation (Luther, 2005). However, as evidenced by cyclic voltammetry (E_{01}) alone, the organic ligand-free interface is kinetically inhibited, showing negligible faradaic activity. Substantial Mn removal observed in this magnesian rhodochrosite-forming experiment (Table 1) thus acts as a control for readily occurring, non-electrochemical Mn-carbonate precipitation. In contrast, functionalization in E_{11} enables the quasi-reversible regeneration of Mn(III) in the system (Fig. 3), isolating a fraction of it from precipitation. This results in lower net Mn removal (Table 1), confirming that the carboxyl ligand field induces kinetic stabilization of Mn(III) in the hydrogel and modulates progressive Mn (II) incorporation in carbonate. The ligands allow the electrode to reductively cycle Mn(III), sustaining the redox engine (Fig. 9A-B), while avoiding the irreversible electroactive reactant loss observed in E_{01}. Thus, the organic matrix (alginate) transforms the system from a passive chemical sink into an active electrochemical engine (Eq. (3)):

$$[\text{R-COO-Mn}^{\text{III}}(\text{OH})] + e^- + H^+ \leftrightarrow [\text{R-COO-Mn}^{\text{II}}] + H_2O \quad (3)$$

4.2.2. *pH sensitivity and the lower pH limit of the proposed mechanism*

The carboxyl functionalization component of the mechanism is effectively pH-independent. At pH 8–10, well above the alginate p*Ka* (Petrash et al., 2011), the bulk of deprotonated carboxyl groups responsible for inner-sphere Mn(III) stabilization remain available. The mechanism proposed here, however, has two pH dependencies. First, the Mn(II)/Mn(III) redox couple is pH-dependent (Fig. S6). Towards pH 8, the Mn(II)/Mn(III) boundary shifts and the potential window required to drive oxidative Mn(II) cycling without crossing into irreversible Mn (IV) oxide territory narrows. Thus, although the operational window becomes more restricted at that pH, it might remain thermodynamically accessible but kinetically constrained by much slower oxidation rates of Mn (II), particularly in solutions undersaturated with respect to $MnCO_3$ (Diem and Stumm, 1984). The second related limitation at pH below our chosen experimental envelope is reduced carbonate ion activity ($\{CO_3^{2-}\}$). Given $pKa_2 \approx 10.3$, decreasing pH to 8.0 lowers $\{CO_3^{2-}\}$ by over an order of magnitude at constant DIC, substantially reducing carbonate saturation and the thermodynamic driving force for nucleation from the porewater solution. In our setup, mineralization relies on localized supersaturation generated at the electroactive interface, where proton-coupled Mn redox cycling modulates carbonate speciation. CO_2 degassing may partially offset this effect by shifting carbonate equilibria at the bulk scale. Locally, compensation can be achieved through elevated DIC linked to the ongoing redox fluxes that shift alkalinity, and influence carbonate mineral saturation states. This compensation, common in lithifying microbial mats colonizing peritidal settings (e.g., Petrash et al., 2015), however, appears to vary as similar sedimentary environments can behave differently, reflecting the balance between gross productivity and net heterotrophy as well as the availability of redox-active species (Present et al., 2021). Under such considerations, the mechanism is thus not constrained by the bulk sediment pH observed in alkaline lagoonal or perhaps rift-lake systems—as implemented here, and may extend to a broader spectrum of dolomite-forming settings where a localized benthic manganous condition (i.e., marked by $MnCO_3$ saturation) may transiently develop (Huckriede and Meischner, 1996).

4.3. *Broader geo(bio)logical implications*

4.3.1. *Paleoenvironmental boundary conditions*

The effectiveness of Mn in mediating the proposed redox-templating

mechanism for carbonate nucleation and growth arises from its unique combination of valence-state flexibility, favorable substitution behavior in carbonate lattices, and relatively labile hydration, which together enable interfacial redox cycling and stabilization of reactive intermediates. The Mn redox engine likely operates in natural settings through consortial, spatially stratified microbial assemblages driving oxidation and reduction reactions coupled via diffusion of intermediates (e.g., Petrash et al., 2022). It may also operate through extracellular electron transfer processes involving microorganisms directly interacting with the sedimentary Mn (and Fe) stocks (Nielsen et al., 2010; Jelen et al., 2016). These microbe-mineral interactions involve species of *Geobacter, Pseudomonas, Rhodoferax, Manganitrophus, Siderooxydans* and *Geothrix*, among others. In shallow, O_2-depleted inner shelf settings, anoxygenic phototrophs likely contributed both to Mn cycling and to production of the required carboxylated organic substrates (Daye et al., 2019). Diurnal redox oscillations of 200–400 mV in modern microbial mats (Jørgensen et al., 1979), widely used as study analogues for the functioning of ancient microbial mats, span the Eh window applied here, indicating that our experiments reproduce the magnitude of redox fluctuations at such natural redox-stratified mineralization interfaces (Petrash et al., 2015).

In deep time, the efficacy of the proposed Mn-templating mechanism was contingent upon the distinctive geochemical boundary conditions characteristic of perturbed states of the Earth system (Falkowski et al., 2008). Robust sedimentological indicators, most notably ubiquitous seafloor carbonate cementation, the proliferation of giant ooids and stromatolitic platforms that extended beyond non-evaporative inner shelf settings, collectively attest to Precambrian shallow-marine environments defined by exceptionally high carbonate saturation states (Grotzinger, 1989) that were also observed in the end-of Permian to Early Triassic transition (e.g., Grotzinger and Knoll, 1995; Woods et al., 1999). This framework aligns with classic Earth system models invoking elevated atmospheric CO_2 (e.g., Kasting, 1987), which require tight coupling between weathering-derived cation fluxes and carbonate precipitation, serving as a feedback mechanism (e.g., Kump et al., 2000; West et al., 2005). In ancient transiently high-DIC depositional systems, elevated primary productivity-driven alkalinity generation, coupled with density stratification in the water column, and enhanced influx of weathering-derived base cations (e.g., Ca^{2+}, Mg^{2+}), and oxidants, would have established conditions conducive to episodic redox-set points that activated the authigenic mineralization machinery examined here (see Petrash et al., 2025).

4.3.2. *Mn site occupancy ratio: a mineralogical fingerprint of kutnahoritic templating?*

Evidence from the application of electron paramagnetic resonance (ESR) spectroscopy to dolomite research reveals a profound structural dichotomy that has remained largely overlooked and therefore unresolved for decades. Following the observation by Schindler and Ghose (1970), Lumsden and Lloyd (1984) identified a preference of Mn for the Mg-site (B-site) in ancient dolomites that is stringently coupled to stoichiometry rather than bulk rock Mn contents. They identified two discrete populations: (i) Group A, consisting of non-stoichiometric, Ca-dolomites with a near-invariant Mn^{2+} Mg-site/Ca-site occupancy ratio of ~5 ± 2, and (ii) Group B, comprising stoichiometric specimens, largely from inner-shelf, evaporitic depositional settings, with ratios spanning from 5 to nearly 70, mean ~30 (Fig. 10A). Interestingly, in one extreme modern lacustrine setting in Minnesota, USA, where stoichiometric dolomite and Mn carbonates form, the ratio was considerably higher (Lumsden and Lloyd, 1984,1989). Critically, Lumsden and Lloyd (1989) concluded that stoichiometric Group B dolomites may possess a common origin, involving a "possibly kinetically controlled mechanism" of Mn and Mg crystal lattice co-incorporation. This observation aligns precisely with the Mn engine presented in this study.

The distinct behaviour of Lumsden and Lloyd's populations possibly reflects divergent paragenetic pathways governed by the presence (or absence) of a Mn-mediated "structural chaperone"; apparently absent in modern Ca-dolomite forming sabkha settings, and in the normal-marine subtidal dolomite-forming ones (Lumsden and Lloyd, 1989; Fig. 10A). The slightly elevated but invariant ratio observed in the few ancient

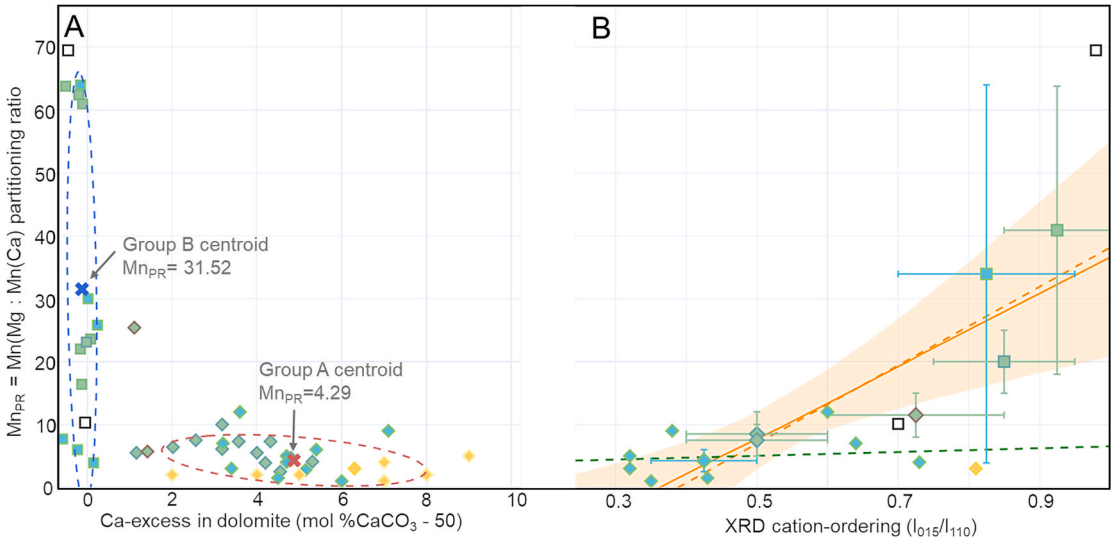

Fig. 10. Relationship between Mn partitioning, cation ordering, and stoichiometry in Phanerozoic dolomite populations (after Lumsden and Lloyd, 1984,1989). (A) Distribution of dolomite populations in stoichiometric–partitioning space, defined by Ca excess (mol% $CaCO_3$ – 50) versus Mn(Mg)/Mn(Ca) partitioning ratio. The grouping denotes near-stoichiometric (blue) and Ca-rich, non-stoichiometric (red) domains. Group B dolomites cluster within the near-stoichiometric field and show elevated Mn partitioning into Mg sites, whereas Group A and associated outliers (including subtidal and modern analogs) define a continuum toward Ca-rich compositions with lower Mn partitioning. Centroids and confidence ellipses summarize population dispersion. (B) Relationship between Mn(Mg)/Mn(Ca) partitioning ratio and cation ordering (XRD I_{015}/I_{110}). Shelf dolomite populations (Lumsden and Lloyd, 1984) are represented as range-constrained data with Monte Carlo–derived envelopes and median regression, compared to ordinary least squares (OLS) fits. Subtidal samples (Lumsden and Lloyd, 1989) are shown as discrete points with corresponding OLS regression. Shelf populations define a robust trend ($R^2 \approx 0.716$; Monte Carlo median $R^2 = 0.578$; 95% CI: 0.278–0.899]; $p = 0.0016$]), whereas subtidal (DSDP) data define a weaker relationship ($R^2 = 0.02$]; $p = 0.691$), consistent with recrystallization and cation ordering. A self-contained version of this figure, including metadata and statistical outputs, is provided in Supplementary Data 2.

Group A, non-stoichiometric dolomites may have resulted from long-term burial temperature- and/or time-dependent stabilization (Lumsden and Lloyd, 1989), or it could have resulted from a distinct, shallow-burial diagenetic formation pathway that lacked the kinetic driver required to rapidly bridge the $MnCO_3$-$MgCO_3$ miscibility gap towards stable Ca-bearing, double-carbonate compositions. Their Group A occurrences may also represent standard crystallization pathways in dysoxic diagenetic settings, where Mn^{2+} is rather a passive substituent.

Their Group B dolomites, on the other hand, recorded their own catalytic ancestry driven by a different redox state, one that facilitates an out-of-equilibrium formation with rapid nucleation and stabilization mediated by the metastable (pseudo-)kutnahoritic scaffold. This formation path ultimately resulted in higher stoichiometry as the system lowers its total free energy by replacing "high-energy" cation defects that distort the structure (such as Ca on a Mg-site), but not necessarily higher cation order—as per the classic I_{015}/I_{110} metric (Fig. 10B), since the Mn in the Mg-site also causes attenuation of the superlattice reflections. The alternative formation path, more commonly observed in Group A, subtidal dolomites (Lumsden and Lloyd, 1989), results in a Mn Mg-to-Ca-site occupancy ratio that approaches near-equilibrium partitioning (Fig. 10B; Kretz, 1982).

Consequently, the Mg-site/Ca-site Mn ratio may serve as a diagnostic criterion for the model presented here. The fact that many of the Group B specimens documented by Lumsden and Lloyd (1984) and Lumsden and Lloyd (1989) are predominantly inner-shelf, evaporite-related deposits of Paleozoic age and consist of very fine-crystalline dolomite (e.g., Montañez and Read, 1992; Abegg, 1992; Manche and Kaczmarek, 2021; Supplementary Data 2) suggests that the diagnostic criterion for Mn catalysis can be preserved across a range of burial diagenetic contexts. The criterion, however, has not yet been systematically applied to the Precambrian successions. Whether Group B-type Mg-site/Ca-site ratios are preserved in well-characterized Proterozoic fabric-retentive dolomicrite facies, formed in independently documented, Mn-stratified basins could be a key geological test of our model.

4.3.3. *A potential link between Mn cycling and ancient syndepositional dolostones*

The catalytic mechanism examined here may have acted as a driver for the massive, basin-wide, microbialitic, fabric-retentive dolostones characteristic of Precambrian carbonate platforms (see Grotzinger, 1989). These deposits, historically interpreted as primary precipitates (Tucker, 1982), are now more widely viewed as syndepositional in origin (Hood et al., 2011). Although such facies dominate the Precambrian carbonate rock record, they also recur in the Phanerozoic during intervals of major environmental perturbation, reflecting transient re-establishment of Precambrian-like carbonate factories (Grotzinger and Knoll, 1995).

With the crystal-to-facies link established, the lithostratigraphic and

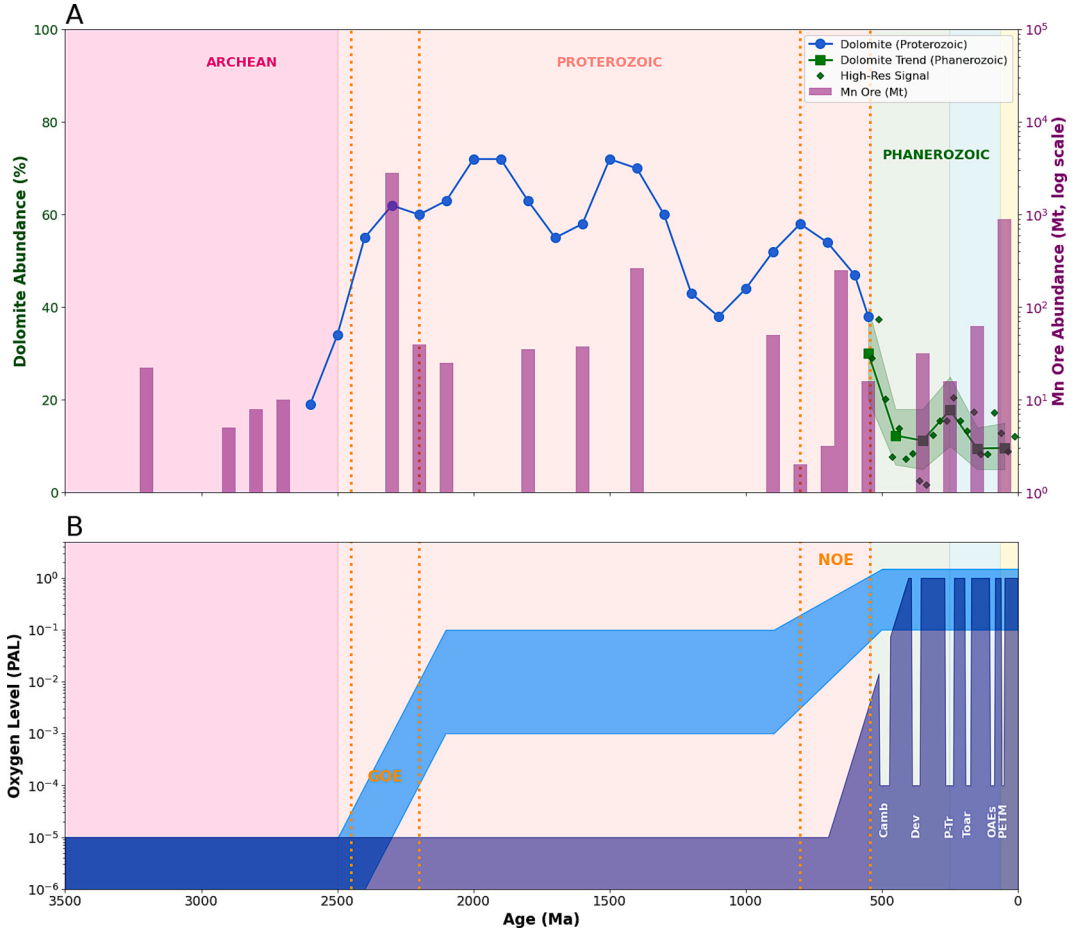

Fig. 11. Integrated evolution of global ocean redox conditions, carbonate mineralogy, and manganese deposition. (A) Secular trends in dolomite abundance (blue: Proterozoic; green: Phanerozoic mean ± SD; derived from Shang, 2023; Li et al., 2021) plotted against Mn ore deposits (purple bars; Robbins et al., 2023). Note the strong co-occurrence of dolomite peaks with Mn pulses in the Precambrian. (B) Evolution of oxygenation states (pO_2). Surface envelopes are calibrated to Chen et al. (2022). The deep ocean tracks surface conditions in the Mesoproterozoic but decouples during high-amplitude redox fluctuations: (i) the Great Oxidation Event (GOE) and Huronian glaciations; (ii) the Lomagundi-Jatuli overshoot; (iii) the Shunga Event oxygen crash; and (iv) the Neoproterozoic Oxygenation Event (NOE). In the Phanerozoic, the deep-water "Mn-pump" is largely suppressed, re-emerging only during transient Ocean Anoxic Events (e.g., P-Tr, Toarcian, K-OAEs) where deep waters dropped to <1% surface saturation. Refer to Supplementary Data 3 for details.

sedimentological record can be assessed for macroscopic evidence of Mn catalysis. Fig. 11A compares the temporal distribution of massive dolostone intervals (Li et al., 2021; Shang, 2023) with pulses of sedimentary manganese deposition (Spinks et al., 2023; Robbins et al., 2023), providing a first-order test of the predicted Mn–dolomite coupling. In the Precambrian, dolostone abundance and sedimentary Mn deposition show a positive monotonic relationship ($\rho = 0.50$; Supplementary Data 3). Although this relationship is constrained by preservation bias and the discontinuous nature of ancient abundance compilations (Petrash et al., 2017), it supports a coupling between redox stratification, Mn accumulation, and seawater chemistry conducive to widespread syndiagenetic dolomite formation.

This coupling is most apparent during the Paleoproterozoic (~2.3–2.05 Ga), when Mn-shuttle-driven processes would have operated efficiently and kutnahorite occurs within massive fabric-retentive dolostone successions, for example in the Fennoscandian Shield (Préat et al., 2011; Nzamba et al., 2026). Evidence for Mn cycling persisted into the Mesoproterozoic, despite increasing euxinia and tectonic quiescence that may have limited long-range Mn(II) transport and large-scale Mn ore formation (Poulton et al., 2010; Planavsky et al., 2014; Robbins et al., 2023). Recent examination of Mesoproterozoic sedimentary records has revealed vigorous Mn cycling in several redox-stratified shallow-marine settings (Spinks et al., 2023; Song et al., 2023; Xu et al., 2025). Among these, the McArthur Basin is notable for localized preservation of delicate fabrics, including Mn-enriched early eukaryote cell structures in the Amelia and Mara dolomite series (Muir, 1976,1983). Because dynamic redox stratification is a prerequisite for sedimentary Mn enrichment (Huckriede and Meischner, 1996), and because preservation of delicate cellular fabrics requires early fine-crystalline dolomite stabilization, these deposits are consistent with an early-forming pathway distinct from multistage burial dissolution-reprecipitation. This pathway was perhaps consistent with a weakly oxidizing Mesoproterozoic Earth in which Mn cycling was active but not conducive to extensive Mn(IV) oxide accumulation.

The controls highlighted above re-emerged more widely during the Neoproterozoic. Then, elevated pCO_2, enhanced weathering-derived cation fluxes, increased shallow-marine productivity, and sluggish circulation promoted non-steady-state early diagenetic conditions (*sensu* Berner, 1980), expressed as chemically distinct interfacial environments in the shallow-marine water column and its sediments. This combined set of conditions favored extensive deposition of syndiagenetic, fabric-retentive dolomite (e.g., Liang et al., 2025; Fang and Xu, 2022; Cai et al., 2023; Hood et al., 2011; Hood and Wallace, 2014; Stacey et al., 2023).

Several Paleozoic intervals featuring the conditions described above are potentially relevant, but their interpretation is complicated by multistage dolomitization and recrystallization, which can obscure primary Mn-partitioning signatures when both fluid- and rock-buffered diagenetic conditions influence the crystal stabilization path (Immenhauser, 2022). The most striking Phanerozoic recurrence of this pattern, however, is recorded in shallow-marine microbial carbonate successions deposited during the end-Permian–Triassic transition (e.g., Aljinović et al., 2025; Liu et al., 2026). During this interval of extended post-extinction redox instability (Rampino and Caldeira, 2005; Li et al., 2025; Taylor et al., 2026), shallow-marine water columns locally developed manganous conditions (Müller et al., 2023). The prevailing epicontinental redox structure was spatially heterogeneous, with persistent anoxia mainly restricted to deeper slope settings, whereas shallow-marine environments experienced episodic redox oscillations linked to transient incursions of anoxic deep waters (Algeo and Twitchett, 2010; Sun, 2024). This provides a relevant Phanerozoic test case for evaluating whether transient re-establishment of Mn-rich, redox-stratified conditions reactivated a mechanism apparently more characteristic of earlier Earth coastal environments.

4.3.4. *Phanerozoic decoupling and restriction to transitional and continental basins*

In contrast to the Precambrian positive Mn-ore-dolomite-abundance association, the Phanerozoic record shows a negative correlation between dolomite and manganese ore abundance ($\rho = -0.80$; Supplementary Data 3). This reversal marks the progressive decoupling of shallow-water Mn cycling from the loci of peritidal dolomitization as ocean oxygenation advanced. In oxygenated oceans, the drivers of massive manganese carbonate precipitation, including subtidal redox boundaries in the water column, became increasingly separated from shallow carbonate-platform environments where fabric-retentive dolomite formed. This general trend was nevertheless punctuated during specific Paleozoic and Mesozoic intervals, and more rarely in the Cenozoic, when oceanographic conditions necessary for shallow-marine Mn cycling were transiently re-established (Hsü and McKenzie, 1985; Zhang et al., 2020; Li et al., 2021; Reershemius and Planavsky, 2021; Robbins et al., 2023).

Our mechanism therefore provides a framework for re-thinking the episodic emergence, restriction, and decline of widespread fabric-retentive dolomite in the Phanerozoic. As the Earth system transitioned toward a fully oxygenated state (Fig. 10B), deep-ocean ventilation disrupted the shallow-water Mn shuttle (Spinks et al., 2023; Chen et al., 2023; Robbins et al., 2023). Mn carbonates progressively gave way to oxidized Mn phases (Johnson et al., 2016), while dolomite formation became increasingly restricted to transitional and continental environments.

The presence of ordered, stoichiometric-trending post-Pliocene sabkha-type dolomite (Chafetz et al., 1999) indicates that the bio/geochemical conditions envisioned here may have been locally maintained in some Neogene coastal settings, particularly where favorable sedimentary Mn influx produced relatively Mn-enriched deposits (Chafetz and Rush, 1994). However, in the modern Dohat Faishakh sabkha of Qatar, Bontognali et al. (2026) report protodolomite formation under circumneutral bulk porewater pH, outside the physicochemical window discussed in Section 4.2.2. Under these conditions, Mn stocks would be expected to be largely immobilized as Mn(IV) oxyhydroxides under oscillating redox conditions (Fig. S6). The absence of trace metal data and microsensor measurements therefore precludes direct assessment of the extent to which the proposed mechanism operates in this classic modern dolomite-forming sabkha setting. Redox coupling with the sulfur cycle during early burial may also play a role (e.g., Petrash et al., 2015).

Although the Mn-templating mechanism for dolomite appears to have largely retreated from Neogene shallow-marine settings, it may have persisted in restricted continental systems, including rift, playa, and stratified lakes (e.g., McCormack et al., 2024; Petrash et al., 2025; *cf.* Chen et al., 2023; Xu et al., 2025). Stratified lacustrine systems characterized by dissolved transition-metal accumulation provide a particularly relevant analogue because they sustain redox gradients, vigorous Mn cycling, and authigenic seasonal precipitation of rhodochrosite and (pseudo)kutnahorite (Dean, 2002; Stevens et al., 2000; Wittkop et al., 2020). Such lakes are commonly used as analogues for ancient redox-stratified oceans (Swanner et al., 2020), while the Minnesota examples are additionally supplied by Mn fluxes from Precambrian bedrock catchments, sustaining Mn-rich depositional conditions (Wittkop et al., 2020). Remarkably, stoichiometric dolomite with exceptionally high Mn occupancy in the Mg-site relative to the Ca-site (>210) has been documented in Elk Lake (Lumsden and Lloyd, 1984, 1989; Dean, 2002). This extreme site-partitioning value is consistent with structurally controlled Mn incorporation inherited from a pseudo-kutnahoritic precursor, rather than simple control by bulk Mn availability.

Finally, our observation that synthetic Mn-carbonate phases can form rapidly is consistent with modern lacustrine systems where vigorous Mn cycling is seasonally established. Together, our results and these sedimentological observations indicate that Mn-carbonate

precipitation kinetics are not inherently limiting when oscillating redox potentials, dissolved Mn^{2+} availability, and carboxylated organic substrates coexist at a metastable mineralization front. Such conditions occur simultaneously in natural biogeochemical systems but are necessarily simplified in inorganic experiments designed to isolate individual kinetic parameters (e.g., Jiang et al., 2026).

4.4. Future experimental work

A technical limitation of the present study is the sub-optimal electron transparency of the FIB lamellae prepared from the inherently friable, polycrystalline spheroid products. Relative thickness mapping reveals t $(\lambda)^{-1}$ values of 0.86–0.88 in the dolomitic cortex regions, where 59 to 64% of incident electrons undergo inelastic scattering, likely obscuring any faint b-type superlattice reflections that would confirm incipient cation ordering. Future work must prioritize optimizing ion polishing protocols to achieve $t(\lambda)^{-1} < 0.5$ in targeted cortex domains, and the systematic identification of rare single-crystal domains within the polycrystalline aggregates suitable for tilt-series SAED analysis. Energy-filtered SAED using a zero-loss window (e.g., Oleshko et al., 1998) would reduce contributions from inelastically scattered electrons and improve diffraction-ring contrast. Resolving whether the substitutionally disordered cortices contain domains of incipient cation ordering remains an important outstanding crystallographic question.

Future work may also evaluate whether variants of the mechanism proposed here could operate, under specific geochemical conditions, with other transition metals or through metastable non-redox-active precursor phases. For example, Fe may contribute to dolomite-group carbonate stabilization through structural substitution, particularly under restricted ferruginous and dolomite-saturated conditions (e.g., Boglaienko et al., 2026). However, Fe is unlikely to operate as a direct analogue of Mn because Fe is commonly immobilized rapidly as oxides or sulfides, limiting reversible interfacial redox cycling conducive to dolomite (Petrash et al., 2025). In those settings where redox stratification occurs in the water column, however, iron is central to the sedimentary redox cycling of Mn. Likewise, other redox-independent metastable intermediates may contribute to carbonate templating. Mg-silicate phases, for example, are commonly associated with dolomite formation in saline sedimentary systems influenced by biogeochemical processes (Pace et al., 2016; Fang et al., 2023; Chen et al., 2024).

4.5. Testable rock-record predictions of the Mn-templating model

The most direct test of the kutnahoritic templating model in fabric-retentive dolostones is the Mn sublattice occupancy pattern defined by Lumsden and Lloyd (1984) and Lumsden and Lloyd (1989). The model predicts elevated Mn^{2+} occupancy of the Mg-site relative to the Ca-site in ancient fabric-retentive dolostones, preserved across diagenetic conditions (Lumsden and Lloyd, 1997). This criterion remains largely untested in Precambrian successions. The key question is whether Group B–type Mg-site/Ca-site ratios occur in Proterozoic dolomicrites formed in Mn-stratified basins, which would indicate structural inheritance from a kutnahoritic template rather than simple control by fluid Mn composition. Testing this prediction requires ESR analysis of three populations: (1) Precambrian fabric-retentive dolomicrites from Mn-stratified basins, including the Francevillian, McArthur Basin, and Cryogenian–Ediacaran cap-carbonate-bearing basins of South China; (2) inner-shelf dolomicrites formed during transient Phanerozoic Mn stratification; and (3) replacive, coarsely crystalline dolostones from the same basins. The model predicts Group B ratios in the first two populations and invariant Group A ratios (~5) in the third, independent of bulk Mn.

ESR limitations constrain this test. Calcite cements and secondary calcite phases, common in dolostone successions, can cause spectral overlap that obscures Mn site assignment, while Fe^{3+} produces background signals that hinder separation of Mg- and Ca-site Mn. These limitations excluded many samples from the original ESR datasets, and the subsequent pooling of dolomites from diverse paragenetic settings obscured the relationship between Mn site partitioning, depositional environment, and formation pathway (i.e., Lumsden and Lloyd, 1997). A combined high-resolution X-ray powder diffraction (HR-XRPD), total scattering pair distribution function (PDF), and Mn K-edge extended X-ray absorption fine structure spectroscopy (EXAFS) approach can overcome these constraints. PDF analysis evaluates short-range order, whereas EXAFS directly resolves Mn coordination and site occupancy. Together, these methods link crystallinity, local structure, and Mn partitioning, enabling a rigorous test of whether preferential Mn occupancy of the Mg site correlates with ordered, stoichiometric deep-time dolomicrites.

5. Conclusions

We demonstrate that coupling manganese redox cycling with carboxyl functionalization unlocks a kinetically favourable, non-classical pathway for the low-temperature formation of manganoan, dolomite-group minerals. Electrochemical valence-state modulation accelerates Mn incorporation by over 60% compared to passive controls, stabilizing a metastable kutnahoritic precursor whose lower cationic mismatch ratio ($R_{Ca}/R_{Mn} \sim 1.20$ *vs.* $R_{Ca}/R_{Mg} \sim 1.38$), given the faster Mn^{2+} desolvation kinetics, circumvents the activation energy barrier that stalls direct Mg^{2+} incorporation in dolomite's B site. Nanostructural characterization reveals that this precursor serves as an isostructural scaffold enabling the semi-oriented nanoparticle attachment and heteroepitaxial overgrowth of substitutionally disordered dolomite cortices within less than 24 h. The mesocrystalline architectures produced by this pathway provide a physical explanation for fabric retention in syndepositional dolostones, i.e., compositional evolution proceeding through particle assembly preserves primary aggregate morphology. Mechanistically, the driving force is a proton-driven cation pump, electrochemical in character: (i) anodic Mn(II) oxidation acidifies the hydrogel-electrode interface, releasing crosslinked Mg^{2+} and Ca^{2+} that can co-precipitate at the growing surface, while (ii) carboxyl functionalization acting as an inner-sphere ligand field suppresses Mn(III) disproportionation, transforming the organic matrix from passive template to active kinetic stabilizer. This can enable dissolution-reprecipitation only at interfacial loci along the spherule growth front, allowing cation reshuffling as the crystal corrects during aging. This coupled, out-of-equilibrium mechanism resolves both the kinetic barrier and the thermodynamic miscibility gap simultaneously, and, at the fine-crystal scale, operates through three core processes: (i) the system lowers its total free energy by replacing "high-energy" cation defects (like Mn on a Ca-site) with the "low-energy" ordered configuration; (ii) at the interface, the lattice rejects excess Ca (which is larger and distorts the structure) in favor of Mg, driving the chemistry toward the ideal 50:50 ratio, and (iii) because this exchange is restricted to the nanoscale boundary (the spherulite growth front), the primary laminar textures and fine grain (dolomicrite) size remain intact, avoiding the destructive "ripening" of bulk recrystallization. At the geological scale, the model may provide a relevant framework for assessing the stratigraphic distribution of fabric-retentive dolostone. Their pervasiveness in the Precambrian reflects the widespread availability of dissolved Mn(II) in redox-stratified ancient basins, while their increasingly punctuated distribution in the Phanerozoic reflects the progressive decoupling of the shallow-water Mn^{2+} reservoir from carbonate platforms by global oxygenation.

6. Data availability

Raw data and Python scripts are available through Zenodo at: 10.5281/zenodo.20158140

CRediT authorship contribution statement

Daniel A. Petrash: Writing – review & editing, Writing – original draft, Visualization, Validation, Supervision, Software, Resources, Project administration, Methodology, Investigation, Funding acquisition, Formal analysis, Data curation, Conceptualization. **Astolfo Valero:** Writing – original draft, Methodology, Data curation. **Or M. Bialik:** Writing – original draft, Validation, Investigation. **Yihang Fang:** Writing – original draft, Visualization, Validation, Formal analysis. **Maartje Hamers:** Visualization, Data curation. **Travis B. Meador:** Writing – original draft, Validation. **Tomaso R.R. Bontognali:** Writing – original draft, Validation, Investigation, Conceptualization. **Michael Ernst Böttcher:** Writing – original draft, Validation, Investigation, Conceptualization. **Oliver Plümper:** Writing – review & editing, Writing – original draft, Validation, Resources, Funding acquisition.

Declaration of competing interest

The authors declare that they have no known competing financial interests or personal relationships that could have appeared to influence the work reported in this paper.

Acknowledgements

The authors thank Chad Wittkop, an anonymous reviewer and Associate Editor Karim Benzerara for their thoughtful feedback and constructive guidance. Their combined inputs helped refine the manuscript and improve its presentation. This is a contribution to the Strategic Research Plan of the Czech Geological Survey (DKRVO/CGS 2023-2027, IP311670). This project has received funding from the European Union's Horizon Europe research and innovation programme under grant agreement 101131765 (EXCITE^2) for Transnational Access conducted at the Advanced Microscopy Facilities, Utrecht University. Views and opinions expressed are however those of the authors only and do not necessarily reflect those of the EU or the European Commission. Neither the EU nor the granting authority can be held responsible for them. TBM, AV and DAP gratefully acknowledge partial support from the Czech Science Foundation under grant 24-12587S to TBM. We thank František Laufek for conducting the XRD analysis of the residual solid phase, and Alireza Chogani for support during FIB-SEM preparation and (S)TEM analyses.

Appendix A. Supplementary material

The supplementary material consists of three supplementary data files. Supplementary Data 1, which includes: (i) mineralogical characterization of residual assemblages, i.e., BSEM and XRD data of aragonite and dypingite; (ii) HRTEM micrographs and FFT patterns quantifying lattice planes and mosaic fabric misorientations; (iii) MnEdgeNet results confirming Mn(II) oxidation state homogeneity; (iv) PHREEQC-derived saturation indices and Eh-pH stability diagrams for the Mn-water system; (v) Supplementary Note S1: A Nernst-Planck approximation quantifying interfacial pH oscillations and their impact on dolomite supersaturation; (vi) Supplementary Note S2: A compendium of sedimentary units, from the Paleoproterozoic to the Holocene, serving as geological test cases. In addition, Supplementary Data 2 is an HTML version of Fig. 10, containing point-specific metadata, and Supplementary Data 3 is a self-contained Python script containing data used for analysis and visualization of Mn ore *vs.* dolomite abundance through deep time. Supplementary material to this article can be found online at https://doi.org/10.1016/j.gca.2026.05.034.

References

Abegg, F.E., 1992. Lithostratigraphy, depositional environments, and sequence stratigraphy of the St. Louis and Ste. Genevieve limestones (Upper Mississippian), southwestern Kansas. Unpubl. Ph.D. dissertation, Department of Geology, University of Kansas, Lawrence, 206 pp. (Available as Kansas Geological Survey, Open-File Report 92-42.).

Al Disi, Z.A., Zouari, N., Bontognali, T.R., 2024. Dissolved silicon as a beneficial factor for biomineralization of disordered dolomite by a halophilic cyanobacterium. Chem. Geol. 670, 122435.

Algeo, T.J., Twitchett, R.J., 2010. Anomalous Early Triassic sediment fluxes due to elevated weathering rates and their biological consequences. Geology 38, 1023–1026.

Aljinović, D., Richoz, S., Smirčić, D., Chen, Y., Nestell, G., Jazvac, I., Petrash, D.A., 2025. Features and dolomitizing mechanisms in inner platform facies across the Permian–Triassic boundary (External Dinarides, Croatia). Sedimentology 72, 822–843.

Arvidson, R.S., Mackenzie, F.T., 1999. The dolomite problem: control of precipitation kinetics by temperature and saturation state. Am. J. Sci. 299 (4), 257–288.

Bard, A.J., Faulkner, L.R., 2011. Electrochemical Methods: Fundamentals and Applications, 2nd ed. John Wiley & Sons, Hoboken, 864 pp. [mostly Ch. 1]).

Berner, R.A., 1980. Early Diagenesis: A Theoretical Approach. Princeton University Press, Princeton, NJ.

Bischoff, J.L., 1968. Kinetics of calcite nucleation: magnesium ion inhibition and ionic strength catalysis. J. Geophys. Res. 73, 3315–3322.

Boglaienko, D.V., Prange, M.P., Stanfield, C.H., Mergelsberg, S.T., Latta, D.E., Li, X., Kerisit, S.N., Schaef, H.T., Rosso, K.M., Miller, Q.R.S., 2026. Cation site occupancy in natural ferroan double carbonates via mössbauer and Fe K-edge X-ray absorption spectroscopy. Inorg. Chem. 65, 5986–5994.

Bontognali, T.R.R., Vasconcelos, C., Warthmann, R.J., Bernasconi, S.M., Dupraz, C., Strohmenger, C.J., McKenzie, J.A., 2010. Dolomite formation within microbial mats in the coastal sabkha of Abu Dhabi (United Arab Emirates). Sedimentology 57, 824–844.

Bontognali, T.R.R., 2019. Anoxygenic phototrophs and the forgotten art of making dolomite. Geology 47, 591–592.

Bontognali, T.R.R., Al Disi, Z., Dittrich, M., DiLoreto, Z., Bernasconi, S.M., Sadooni, F., Al-Kuwari, H.-S., 2026. An identity card for sabkha dolomite. Dep. Rec. 12, e70049.

Böttcher, M.E., 1998. Manganese(II) partitioning during experimental precipitation of rhodochrosite-calcite solid-solutions from aqueous solutions. Mar. Chem. 62, 287–297.

Böttcher, M.E., Dietzel, M., 2010. Metal-ion partitioning during low-temperature precipitation and dissolution of anhydrous carbonates and sulfates. EMU Notes Min. 10, 139–187.

Cai, Y., Wallace, M.W., Hua, H., Hood, A., 2023. Interlinked marine cycles of methane, manganese, and sulfate in the post-Marinoan Doushantuo cap dolostone. Geochim. Cosmochim. Acta 346, 160–179.

Chafetz, H.S., Rush, P.F., 1994. Diagenetically altered sabkha-type Pleistocene dolomite from the Arabian Gulf. Sedimentology 41, 409–421.

Chafetz, H.S., Imerito-Tetzlaff, A.A., Zhang, J., 1999. Stable-isotope and elemental trends in pleistocene sabkha dolomites: descending meteoric water vs. sulfate reduction. J. Sediment. Res. 69, 256–266.

Chang, B., Li, C., Liu, D., Foster, I., Tripati, A., Lloyd, M.K., Immenhauser, A., 2020. Massive formation of early diagenetic dolomite in the Ediacaran ocean: constraints on the "dolomite problem". PNAS 117, 5522–5529.

Chen, G., Cheng, Q., Lyons, T.W., Shen, J., Agterberg, F., Huang, N., Zhao, M., 2022. Reconstructing Earth's atmospheric oxygenation history using machine learning. Nat. Commun. 13, 586.

Chen, F., Wang, Q., Pufahl, P.K., Matheson, E.J., Xian, H., Nan, J., Ma, H., Deng, J., 2023. Carbonate-hosted manganese deposits and ocean anoxia. Earth Planet. Sci. Lett. 622, 118385.

Chen, T., Qiu, X., Liu, D., Papineau, D., Wang, H., Dai, Z., Bontognali, T.R.R., Benzerara, K., 2024. Dissolved silicon as a beneficial factor for biomineralization of disordered dolomite by a halophilic cyanobacterium. Chem. Geol. 670, 122435.

Cölfen, H., Mann, S., 2003. Higher-order organization by mesoscale self-assembly and transformation of hybrid nanostructures. Angew. Chem. Int. Ed. 42, 2350–2365.

Daye, M.E., Klepac-Ceraj, V., Bosak, T., 2019. Anoxygenic phototrophs and the forgotten art of making dolomite. Geology 47, 509–512.

De Yoreo, J.J., Gilbert, P.U.P.A., Sommerdijk, N.A.J.M., Penn, R.L., Whitelam, S., Joester, D., Zhang, H., Rimer, J.D., Navrotsky, A., Banfield, J.F., Wallace, A.F., Michel, F.M., Meldrum, F.C., Cölfen, H., Dove, P., 2015. Crystallization by particle attachment in synthetic, biogenic, and geologic environments. Science 349, 1–9.

Dean, W.E., 2002. A 1500-year record of climatic and environmental change in Elk Lake, Clearwater County, Minnesota II: Geochemistry, mineralogy, and stable isotopes. J. Paleolimnol. 27, 301–319.

Di Loreto, Z.A., Garg, S., Bontognali, T.R., Dittrich, M., 2021. Modern dolomite formation caused by seasonal cycling of oxygenic phototrophs and anoxygenic phototrophs in a hypersaline sabkha. Sci. Rep. 11, 4170.

Diem, D., Stumm, W., 1984. Is dissolved Mn^{2+} being oxidized by O_2 in the absence of Mn-bacteria or surface catalysts? Geochim. Cosmochim. Acta 48, 1571–1573.

Egerton, R.F., 2011. Electron Energy-Loss Spectroscopy in the Electron Microscope, third ed. Springer, New York.

Falkowski, P.G., Fenchel, T., DeLong, E.F., 2008. The microbial engines that drive Earth's biogeochemical cycles. Science 320, 1034–1039.

Fang, Y., Xu, H., 2019. A new approach to quantify ordering state of protodolomite using XRD, TEM, and Z-contrast imaging. J. Sediment. Res. 89, 537–551.

Fang, Y., Xu, H., 2022. Coupled dolomite and silica precipitation from continental weathering during deglaciation of the Marinoan Snowball Earth. Precambr. Res. 380, 106824.

Fang, Y., Hobbs, F., Yang, Y., Xu, H., 2023. Dissolved silica-driven dolomite precipitation in the Great Salt Lake, Utah, and its implication for dolomite formation environments. Sedimentology 70, 1328–1347.
Goldsmith, J.R., Graf, D.L., 1960. Subsolidus relations in the system $CaCO_3$-$MgCO_3$-MnCO3. J. Geol. 68, 324–335.
Goldsmith, J.R., 1983. In: Reeder, R.J. (Ed.), Carbonates: Mineralogy and Chemistry. Reviews in Mineralogy, 11. Mineralogical Society of America, Washington, D.C, pp. 49–76.
Graf, D.L., Goldsmith, J.R., 1956. Some hydrothermal syntheses of dolomite and protodolomite. J. Geol. 64, 173–186.
Gránásy, L., Pusztai, T., Tegze, G., Warren, J.A., Douglas, J.F., 2005. Growth and form of spherulites. Phys. Rev. E 72, 011605.
Gregg, J.M., Sibley, D.F., 1984. Epigenetic dolomitization and the origin of xenotopic dolomite texture. J. Sediment. Petrol. 54, 908–931.
Gregg, J.M., Bish, D.L., Kaczmarek, S.E., Machel, H.G., 2015. Mineralogy, nucleation and growth of dolomite in the laboratory and sedimentary environment: a review. Sedimentology 62, 1749–1769.
Grotzinger, J.P., 1989. Facies and evolution of Precambrian carbonate depositional systems: Emergence of the modern platform archetype. *In*: Crevello, P.D., Read, J.F., Sarg, R.J., Wilson, J.L. (Eds.), Controls on Carbonate Platform and Basin Development. *SEPM Spec. Publ.* 44, 79–106.
Grotzinger, J.P., Knoll, A.H., 1995. Anomalous carbonate precipitates: is the Precambrian the key to the Permian? PALAIOS 10, 578–596.
Han, Z., Zhang, F., Farfan, G.A., Xu, H., 2024. Dissolved Mn2+ promotes microbially-catalyzed protodolomite precipitation in brackish oxidized water. Chem. Geol. 650, 121986.
Helm, L., Merbach, A.E., 2005. Inorganic and bioinorganic solvent exchange mechanisms. Chem. Rev. 105, 1923–1959.
Higgins, S.R., Hu, X., 2005. Self-limiting growth on dolomite (104) surfaces. Geochim. Cosmochim. Acta 69, 2085–2094.
Hood, A.S., Wallace, M.W., Drysdale, R.N., 2011. Neoproterozoic aragonite–dolomite seas? Widespread marine dolomite precipitation in Cryogenian reef complexes. Geology 39, 871–874.
Hood, A.S., Wallace, M.W., 2014. Marine cements reveal the structure of an anoxic, ferruginous Neoproterozoic ocean. J. Geol. Soc. London 171, 741–744.
Hsü, K.J., McKenzie, J.A., 1985. A "Strangelove" ocean in the earliest Tertiary. In: E.T. Sundquist, W.S. Broecker (Eds.), The carbon cycle and atmospheric CO2: Natural variations Archean to present *Geophysical Monograph Series* 32, 487–492.
Huckriede, H., Meischner, D., 1996. Origin and environment of manganese-rich sediments within black-shale basins. Geochim. Cosmochim. Acta 60 (8), 1399–1413.
Immenhauser, A., 2022. On the delimitation of the carbonate burial realm. Dep. Rec. 8, 110–137.
Ingerson, E., 1962. Problems of the geochemistry of sedimentary carbonate rocks. Geochim. Cosmochim. Acta 26, 815–847.
Jakob, K.S., Walsh, A., Reuter, K., Margraf, J.T., 2025. Learning crystallographic disorder: bridging prediction and experiment in materials discovery. Adv. Mater., e14226
Jelen, B.I., Giovannelli, D., Falkowski, P.G., 2016. The role of microbial electron transfer in the coevolution of the biosphere and geosphere. Annu. Rev. Microbiol. 70, 45–62.
Ji, Z., Hu, M., Xin, H.L., 2023. Mn-EdgeNet for accurate decomposition of mixed oxidation states for Mn XAS and EELS L2,3 edges without reference and calibration. Sci. Rep. 13, 14132.
Ji, D., Park, J.M., Oh, M.S., Nguyen, T.L., Shin, H., Kim, S.L., Kim, D., Kim, J., 2022. Superstrong, superstiff, and conductive alginate hydrogels. Nat. Commun. 13, 3019.
Jiang, C.Z., Liu, Z., Tosca, N.J., 2026. Precipitation kinetics and C isotope fractionation of rhodochrosite at 298.15 K. Geochim. Cosmochim. Acta 413, 204–217.
Johnson, J.E., Webb, S.M., Ma, C., Fischer, W.W., 2016. Manganese mineralogy and diagenesis in the sedimentary rock record. Geochim. Cosmochim. Acta 173, 210–231.
Jørgensen, B.B., Revsbech, N.P., Blackburn, T.H., Cohen, Y., 1979. Diurnal cycle of oxygen and sulfide microgradients and microbial photosynthesis in a cyanobacterial mat sediment. *Appl. Environ. Microbiol.* 38, 46–58.
Kaczmarek, S.E., Sibley, D.F., 2014. On the evolution of dolomite stoichiometry and cation order during high-temperature synthesis experiments: an alternative model for the geochemical evolution of natural dolomites. Sed. Geol. 301, 32–43.
Kaczmarek, S.E., Thornton, B.P., 2017. The nature of the dolomite (104) peak, and its implication for interpreting the degree of cation order in high-temperature synthesis experiments. Chem. Geol. 470, 148–161.
Kasting, J.F., 1987. Theoretical constraints on oxygen and carbon dioxide concentrations in the Precambrian atmosphere. Precambr. Res. 34, 205–229.
Katsikopoulos, D., Fernández-González, Á., Prieto, M., 2009. Crystallization behaviour of the (Mn,Ca)CO3 solid solution in silica gel: nucleation, growth and zoning phenomena. Min. Mag. 73, 269–284.
Kretz, R., 1982. A model for the distribution of trace elements between calcite and dolomite. Geochim. Cosmochim. Acta 46, 1979–1981.
Kump, L.R., Brantley, S.L., Arthur, M.A., 2000. Chemical weathering, atmospheric CO_2, and climate. Annu. Rev. Earth Planet. Sci. 28, 611–667.
Li, M., Wignall, P.B., Dai, X., Hu, M., Song, H., 2021. Phanerozoic variation in dolomite abundance linked to oceanic anoxia. Geology 49, 698–702.
Li, Z.-H., Lenton, T.M., Zhang, F.-F., Chen, Z.-Q., Daines, S.J., 2025. Earth system instability amplified biogeochemical oscillations following the end-Permian mass extinction. Nat. Commun. 16, 3703.
Liang, Z., Ning, M., Li, C., Wang, X., Xing, C., 2025. Elemental mapping reveals selective dolomitization in tonian stromatolites: implications for early diagenesis and paleoenvironmental proxies. G^3 26 e2025GC012653.
Lippmann, F., 1973. The System CaCO3-MgCO3. Lippmann, F. (Ed.) Sedimentary Carbonate Minerals; Springer, pp 148−190.
Liu, D., Visscher, P.T., Huang, Y., Fang, Q., Pei, Y., Li, Z.-H., Zheng, Z., Chen, Z.-Q., 2026. Redox control on protodolomite formation in post-extinction microbialites: evidence from the Permian−Triassic boundary beds in South China. *Geochim. Cosmochim. Acta* 423, 51–64.
Lumsden, D.N., Lloyd, R.V., 1984. Mn^{2+} distribution in dolomite: evidence from electron spin resonance. Geochim. Cosmochim. Acta 48, 205–210.
Lumsden, D.N., Lloyd, R.V., 1989. Distribution of Mn^{2+} between Ca and Mg sites in dolomite: evidence from ESR spectroscopy. Geochim. Cosmochim. Acta 53, 289–295.
Lumsden, D.N., Lloyd, R.V., 1997. Three dolomites. J. Sediment. Res. 67, 391–396.
Luther, G.W., 2005. Thermodynamics and kinetics of manganese (II) oxidation and Mn (IV) reduction in the environment: two one-electron transfer steps versus a single two-electron step. Geomicrobiol. J. 22, 195–203.
Machel, H.G., 1997. Recrystallization versus neomorphism, and the concept of 'significant recrystallization' in dolomite research. Sed. Geol. 113, 161–168.
Manche, C.J., Kaczmarek, S.E., 2021. A global study of dolomite stoichiometry and cation ordering through the Phanerozoic. J. Sediment. Res. 91, 520–546.
Marcus, Y., 1987. Thermodynamics of ion hydration and its interpretation in terms of a common model. Pure Appl. Chem. 59, 1093–1101.
McCormack, J., Bontognali, T.R.R., Immenhauser, A., Kwiecien, O., 2018. Controls on cyclic formation of Quaternary early diagenetic dolomite. Geophys. Res. Lett. 45, 3625–3634.
McCormack, J., Baldermann, A., Bontognali, T.R.R., Wolf, A., Kwiecien, O., 2024. Hydrochemical mixing-zones trigger dolomite formation in an alkaline lake. Sedimentology 71, 871–886.
McKenzie, J.A., 1991. The dolomite problem; an outstanding controversy. In: *Controversies in Modern Geology: Evolution of Geological Theories in Sedimentology, Earth History and Tectonics*. Academic Press, pp. 37–54.
Meister, P.H., Frisia, S., Dódony, I., Pekker, P., Molnár, Z., Neuhuber, S., Gier, S., Kovács, I., Demény, A., Pósfai, M., 2023. Nanoscale pathway of modern dolomite formation in a shallow, alkaline lake. Cryst. Growth Des. 23, 3202–3212.
Meister, P.H., 2025. Spherulitic mineral growth: auto-deformation, growth front nucleation or semi-oriented attachment? *In: Nucleation and Growth of Sedimentary Minerals* (Eds P.H. Meister, C. Fischer and N. Preto), *Int. Assoc. Sedimentol. Spec. Publ.*, 50, 171–189.
Meng, R., Han, Z., Gao, X., Zhao, Y., Han, C., Han, Y., Yang, R., Li, S., Liu, F., Tucker, M. E., Yan, H., 2024. Dissolved ammonia catalyzes proto-dolomite precipitation at Earth surface temperature. Earth Planet. Sci. Lett. 646, 119012.
Mercedes-Martín, R., Rogerson, M.R., Brasier, A.T., Vonhof, H.B., Prior, T.J., Fellows, S. M., Pedley, H.M., 2016. Growing spherulitic calcite grains in saline, hyperalkaline lakes: experimental evaluation of the effects of Mg-clays and organic acids. Sed. Geol. 335, 93–102.
Montañez, I.P., Read, J.F., 1992. Fluid–rock interaction history during stabilization of early dolomites, Upper Knox Group (lower Ordovician), U.S. Appalachians. J. Sediment. Res. 62, 753–778.D.
Mucci, A., 1988. Manganese uptake during calcite precipitation from seawater: conditions leading to the formation of a pseudo-kutnahorite. Geochim. Cosmochim. Acta 52, 1859–1868.
Mucci, A., 2004. The behavior of mixed Ca–Mn carbonates in water and seawater: controls of manganese concentrations in marine porewaters. Aquat. Geochem. 10, 139–169.
Müller, J., Sun, Y.D., Yang, F., Regelous, M., Joachimski, M.M., 2023. Manganous water column in the Tethys Ocean during the Permian–Triassic transition. Glob. Planet. Change 222, 104067.
Muir, M.D., 1976. Proterozoic microfossils from the Amelia Dolomite, McArthur Basin, Northern Territory. Alcheringa 1, 143–158.
Muir, M.D., 1983. Proterozoic microfossils from the Mara Dolomite Member, Emmerugga Dolomite, McArthur Group, from the Northern Territory, Australia. Bot. J. Linn. Soc. 86, 1–18.
Nielsen, L.P., Risgaard-Petersen, N., Fossing, H., Christensen, P.B., Sayama, M., 2010. Electric currents couple spatially separated biogeochemical processes in marine sediment. Nature 463, 1071–1074.
Nzamba, K.X., Juhkama, H.R., Moussavou, M., Mayika, K.B., Kreitsmann, T., Lepland, A., Prave, A.R., Kirsimäe, K., 2026. Carbonate diagenesis and Mn-carbonate formation in the Paleoproterozoic Francevillian succession (Lastoursville sub-basin) of Gabon. J. Afr. Earth Sc. 235, 105971.
Oleshko, V.P., Howe, J.M., Shukla, S., Seal, S., 1998. Energy-filtered transmission electron microscopy and electron energy-loss spectroscopy of calcium phosphates. Microsc. Res. Tech. 42, 108–122.
Oomori, T., Kitano, Y., 1987. Synthesis of protodolomite from sea water containing dioxane. Geochem. J. 21, 59–65.
Peacor, D.R., Essene, E.J., Gaines, A.M., 1987. Petrologic and crystal-chemical implications of cation order-disorder in kutnahorite [$CaMn(CO_3)_2$]. Am. Mineral. 72, 319–328.
Pace, A., Bourillot, R., Bouton, A., Vennin, E., Galaup, S., Bundeleva, I., Patrier, P., Dupraz, C., Thomazo, C., Sansjofre, P., Yokoyama, Y., Franceschi, M., Anguy, Y., Pigot, L., Virgone, A., Visscher, P.T., 2016. Microbial and diagenetic steps leading to the mineralisation of Great Salt Lake microbialites. Sci. Rep. 6, 31495.
Petrash, D.A., Roeser, P., Kříbek, B., Staudigel, P.T., Bernecker, M., Jačková, I., Čejková, B., Kochergina, Y.V.E., Koubová, M., Křížová, Š., Knésl, I., Laufek, F., Böttcher, M.E., Della Porta, G., Fiebig, J., 2025. Drivers of episodic carbonate cementation during the Miocene Climatic Optimum in a paleolake of the Eger Rift (Czech Republic). Geochim. Cosmochim. Acta 407, 47–66.

Petrash, D.A., Steenbergen, I.M., Valero, A., Meador, T.B., Pačes, T., Thomazo, C., 2022. Aqueous system-level processes and prokaryote assemblages in the ferruginous and sulfate-rich bottom waters of a post-mining lake. Biogeosciences 19, 1723–1751.
Petrash, D.A., Bialik, O.M., Bontognali, T.R., Vasconcelos, C., Roberts, J.A., McKenzie, J. A., Konhauser, K.O., 2017. Microbially catalyzed dolomite formation: from near-surface to burial. Earth Sci. Rev. 171, 558–582.
Petrash, D.A., Lalonde, S.V., González-Arismendi, G., Gordon, R.A., Méndez, J.A., Gingras, M.K., Konhauser, K.O., 2015. Can Mn–S redox cycling drive sedimentary dolomite formation? A hypothesis. Chem Geol. 404, 27–40.
Petrash, D.A., Lalonde, S.V., Raudsepp, M., Konhauser, K.O., 2011. Assessing the importance of organic matrix materials in biofilm chemical reactivity: insights from proton and cadmium adsorption onto the commercially available biopolymer alginate. Geomicrobiol J. 28, 266–273.
Present, T.M., Gomes, M.L., Trower, E.J., Osburn, M.R., Bergmann, K.D., 2021. Non-lithifying microbial ecosystem dissolves peritidal lime sand. Nat. Commun. 12, 3037.
Pina, C.M., Pimentel, C., Crespo, Á., 2022. The dolomite problem: A matter of time. ACS Earth Space Chem. 6, 1468–1471.
Planavsky, N.J., Reinhard, C.T., Wang, X., Thomson, D., McGoldrick, P., Rainbird, R.H., Johnson, T., Fischer, W.W., Lyons, T.W., 2014. Low mid-Proterozoic atmospheric oxygen levels and the delayed rise of animals. Science 346, 635–638.
Poulton, S.W., Fralick, P.W., Canfield, D.E., 2010. Spatial variability in oceanic redox structure 1.8 billion years ago. Nat. Geosci. 3, 486–490.
Préat, A., Bouton, P., Thiéblemont, D., Prian, J.P., Ndounze, S.S., Delpomdor, F., 2011. Paleoproterozoic high $\delta^{13}C$ dolomites from the Lastoursville and Franceville basins (SE Gabon): stratigraphic and synsedimentary subsidence implications. Precambr. Res. 189, 212–228.
Putnis, C. V., Wang, L., Ruiz-Agudo, E., Ruiz-Agudo, C., Renard, F., 2021. Crystallization via nonclassical pathways: Nanoscale imaging of mineral surfaces. In: Zhang, X. (Ed.), Crystallization via Nonclassical Pathways Volume 2: Aggregation, Biomineralization, Imaging & Application. American Chemical Society, pp. 1–35.
Rampino, M.R., Caldeira, K., 2005. Major perturbation of ocean chemistry and a "Strangelove Ocean" after the end-Permian mass extinction. Terra Nova 17, 554–559.
Reeder, R.J., 1983.Crystal chemistry of the rhombohedral carbonates. *In:* Reeder, R.J. (Ed.), Carbonates: Mineralogy and Chemistry. *Reviews in Mineralogy 11,* Mineralogical Society of America, Washington, D.C., pp. 1–47.
Reershemius, T., Planavsky, N.J., 2021. What controls the duration and intensity of ocean anoxic events in the Paleozoic and the Mesozoic? Earth Sci. Rev. 221, 103787.
Ren, M., 2025. Carbonate sedimentation and early diagenesis of the Doushantuo Formation, South China: a window into the terminal Proterozoic. Sed. Geol. 479, 106847.
Robbins, L.J., Fakhraee, M., Smith, A.J.B., Bishop, B.A., Swanner, E.D., Peacock, C.L., Wang, C.L., Planavsky, N.J., Reinhard, C.T., Crowe, S.A., Lyons, T.W., 2023. Manganese oxides, Earth surface oxygenation, and the rise of oxygenic photosynthesis. Earth Sci. Rev. 239, 104368.
Rodriguez-Blanco, J.D., Shaw, S., Benning, L.G., 2015. A route for the direct crystallization of dolomite. Am. Mineral. 100 (5–6), 1172–1181.
Rosenberg, P.E., Foit Jr., F.F., 1979. The stability of dolomite in aqueous solution: an experimental investigation at 25° to 275°C. Geochim. Cosmochim. Acta 43, 951–955.
Schindler, P., Ghose, S., 1970. Electron paramagnetic resonance of Mn^{2+} in dolomite and magnesite, and Mn^{2+} distribution in dolomites. Am. Mineral. 55, 1900–1915.
Shang, H., 2023. Dichotomous effects of oxidative metabolisms: a theoretical perspective on the dolomite problem. Glob. Planet. Change 222, 104041.
Shi, L., Dong, H., Reguera, G., Beyenal, H., Lu, A., Liu, J., Yu, H.-Q., Fredrickson, J.K., 2016. Extracellular electron transfer mechanisms between microorganisms and minerals. Nat. Rev. Microbiol. 14, 651–662.
Silverman, D.N., Lindskog, S., 1988. The catalytic mechanism of carbonic anhydrase: implications of a rate-limiting protolysis of water. Acc. Chem. Res. 21, 30–36.
Slaughter, M., Hill, R.J., 1991. The influence of organic matter in organogenic dolomite formation at various temperatures and pressures. J. Sediment. Res. 61 (2), 296–303.
Song, Y., Bowyer, F.T., Mills, B.J.W., Poulton, S.W., Lenton, T.M., Shields, G.A., 2023. Dynamic redox and nutrient cycling response to climate forcing in the Mesoproterozoic ocean. *Nat. Commun.* 14, 6640.
Spinks, S.C., Sperling, E.A., Thorne, R.L., LaFountain, F., White, A.J.R., Armstrong, J., Woltering, M., Tyler, I.M., 2023. Mesoproterozoic surface oxygenation accompanied major sedimentary manganese deposition at 1.4 and 1.1 Ga. Geobiology 21, 28–43.
Stacey, J., Hood, A.V.S., Wallace, M.W., 2023. Persistent late Tonian shallow marine anoxia and euxinia. Precambr. Res. 397, 107207.
Stevens, L.R., Ito, E., Olson, D.E.L., 2000. Relationship of Mn-carbonates in varved lake-sediments to catchment vegetation in Big Watab Lake, MN, USA. J. Paleolimnol. 24, 199–211.
Sun, Y., 2024. Dynamics of nutrient cycles in the Permian–Triassic oceans. Earth Sci. Rev. 258 (104914), 58.
Swanner, E.D., Lambrecht, N., Wittkop, C., Harding, C., Katsev, S., Torgeson, J., Poulton, S.W., 2020. The biogeochemistry of ferruginous lakes and past ferruginous oceans. Earth-Sci. Rev.
Taylor, K., Rauzi, S., Isson, T., Ibarra, D.E., Hülse, D., Kimmig, S.R., Payne, J.L., Altiner, D., Lehrmann, D.J., Kalderon-Asael, B., Planavsky, N.J., Lau, K.V., 2026. Heterogeneous carbonate lithium isotope records across the end-Permian mass extinction indicate a highly perturbed lithium cycle in the Early Triassic. Am. J. Sci. 326, 5.
Thortenson, D.C., Plummer, L.N., 1977. Equilibrium criteria for two-component solids reacting with fixed composition in an aqueous-phase; example: the magnesian calcite. Am. J. Sci. 277, 1203–1223.
Tordi, P., Ridi, F., Samorì, P., Bonini, M., 2025. Cation-alginate complexes and their hydrogels: a powerful toolkit for the development of next-generation sustainable functional materials. Adv. Funct. Mater. 35, 2416390.
Trichet, J., Defarge, C., 1995. Non-biologically supported organomineralization. Bull. L'institut Océanogr. Monaco 14 (2), 203–236.
Tucker, M.E., 1982. Precambrian dolomites: petrographic and isotopic evidence for primary dolomite formation. Precambr. Res. 17, 1–20.
Usdowski, E., 1989. Synthesis of dolomite and magnesite at 60 °C in the system Ca^{2+}–Mg^{2+}–CO_3^{2-}–Cl^-–H_2O. Naturwissenschaften 76, 374–375.
Vandeginste, V., Snell, O., Hall, M.R., Steer, E., Vandeginste, A., 2019. Acceleration of dolomitization by zinc in saline waters. Nat. Commun. 10, 1851.
Van Tendeloo, G., Amelinckx, S., De Fontaine, D., 1985. On the nature of the 'short–range order' in 1/2{hkl} alloys. Acta Crystallogr. B 41, 281–292.
Wang, D., Wallace, A.F., De Yoreo, J.J., Dove, P.M., 2009. Carboxylated molecules regulate magnesium content of amorphous calcium carbonates during calcification. PNAS 106, 21511–21516.
Warren, J.K., 1990. Sedimentology and mineralogy of dolomitic Coorong lakes, South Australia. J. Sediment. Res. 60, 843–858.
Weber, J.N., 1964. Trace element composition of dolostones and dolomites and its bearing on the dolomite problem. Geochim. Cosmochim. Acta 28, 1817–1868.
West, A.J., Galy, A., Bickle, M., 2005. Tectonic and climatic controls on silicate weathering. Earth Planet. Sci. Lett. 235, 211–228.
Wittkop, C., Swanner, E.D., Grengs, A., Lambrecht, N., Fakhraee, M., Myrbo, A., Bray, A. W., Poulton, S.W., Katsev, S., 2020. Evaluating a primary carbonate pathway for manganese enrichments in reducing environments. Earth Planet. Sci. Lett. 538, 116201.
Wogelius, R.A., Fraser, D.G., Feltham, D.J., Whiteman, M.I., 1992. Trace element zoning in dolomite: proton microprobe data and thermodynamic constraints on fluid compositions. Geochim. Cosmochim. Acta 56 (1), 319–334.
Wolthers, M., Gebauer, D., Demichelis, R., 2025. Early stages of mineral formation in water: from ion pairs to crystals. Elements 21, 18–24.
Woods, A.D., Bottjer, D.J., Mutti, M., Morrison, J., 1999. Lower Triassic large sea-floor carbonate cements: their origin and a mechanism for the prolonged biotic recovery from the end-Permian mass extinction. Geology 27, 645–648.
Xu, L., Yu, W., Konhauser, K.O., Guo, H., Jin, S., Ma, P., Du, Y., 2025. Genesis of manganese-rich deposits in the Mesoproterozoic Gaoyuzhuang Formation, North China: implications for atmospheric redox state and early eukaryote evolution. Palaeogeogr. Palaeoclimatol. Palaeoecol. 668, 112924.
Zempolich, W.G., Baker, P.A., 1993. Experimental and natural mimetic dolomitization of aragonite ooids. J. Sediment. Res. 63, 247–263.
Zhang, F., Xu, H., Konishi, H., Roden, E.E., 2012a. Polysaccharide catalyzed nucleation and growth of disordered dolomite: a potential precursor of sedimentary dolomite. Am. Mineral. 98, 2070–2076.
Zhang, F., Xu, H., Konishi, H., Roden, E.E., 2012b. Dissolved sulfide-catalyzed precipitation of disordered dolomite: implications for the formation mechanism of sedimentary dolomite. Geochim. Cosmochim. Acta 97, 148–165.
Zhang, F., Shen, S.Z., Cui, Y., Lenton, T.M., Dahl, T.W., Zhang, H., Zheng, Q.F., Wang, W., Krainer, K., Anbar, A.D., 2020. Two distinct episodes of marine anoxia during the Permian-Triassic crisis evidenced by uranium isotopes in marine dolostones. Geochim. Cosmochim. Acta 287, 165–179.